Technische Universität München

A lumped parameter model of cerebral blood flow regulation: Applications to simulation of carotid endarterectomy

Jonas Schollenberger

Master's thesis

2015

Supervisors:
Prof. C. Alberto Figueroa
Martin Pfaller, M.Sc.

Institute for Computational Mechanics
Prof. Dr.–Ing. W. A. Wall
Technische Universität München
Boltzmannstraße 15
85748 Garching b. München (Germany)

Own work declaration

Hereby I confirm that this is my own work and I referenced all sources and auxiliary means used and acknowledged any help that I have received from others as appropriate.

(location, date) (signature)

Acknowledgements

I would like to express my deepest gratitude to my advisor, Prof. Alberto Figueroa, for giving me the opportunity to come to the University of Michigan and work with him for my Master thesis project. I am very thankful for his great support, excellent guidance, and immense knowledge during my time in Ann Arbor. Its been a fantastic experience and I look forward to returning to Michigan to continue working on this project.

I would like to thank Prof. Wolfgang Wall for making all this possible by giving me the opportunity to go abroad for my Master thesis project and for providing the introduction to Prof. Figueroa. I would also like to thank Martin Pfaller for supervising my thesis at the Technische Universität München.

Thank you to Dr. Kevin Lau for your advice and moral support throughout my thesis. I would like to thank Prof. Ramon Berguer for assisting me with questions about surgical procedures. I would like to also give special thanks to Prof. Enrique Criado for taking the time to discuss my simulation results.

Thank you to all my fellow labmates in the Computational Vascular Biomechanics Lab: Federica Cuomo, Dr. Miquel Aguirre, Dr. Nan Xiao, and Dr. Sabrina Ben Ahmed for your great support and for all the good times we had together.

Contents

1 Introduction **1**

2 Physiology **5**

2.1 Cerebral vasculature 5

2.1.1 Circle of Willis 5

2.1.2 The Monro-Kellie hypothesis 5

2.1.3 Cerebrospinal fluid 6

2.2 Cerebral autoregulation 7

2.3 Carotid stenosis and endarterectomy 10

3 Methods **15**

3.1 Modeling cerebral blood flow 15

3.1.1 Poiseuille's Law 15

3.1.2 0D-model of the head and neck vessels 16

3.1.3 0D-model of cerebrovascular system 17

3.1.4 Modeling stenosis 24

3.2 Autoregulation model 25

3.3 Implementation in MATLAB 27

4 Results **29**

4.1 Baseline values 29

4.2 Performance and limits of the cerebral autoregulation model 29

4.3 Simulation of cerebral flow autoregulation following carotid clamping during endarterectomy 36

4.3.1 Stenosed right carotid artery 37

4.3.2 Stenosed carotid and vertebral arteries 38

4.3.3 Stenosed carotid and vertebral arteries in combination with a missing right PCoA and contralateral PCA,P1 42

5 Discussion **51**

5.1 0D-model of the cerebrovascular system 51

5.2 Simulation of carotid endarterectomy 53

6 Conclusion and outlook **57**

List of Figures

1 Inferior view of the cerebral arteries forming the circle of Willis . . . 6
2 Structure of the arterial vessel wall . . . 9
3 Stenosis of the carotid artery . . . 11
4 Carotid endarterectomy . . . 12
5 Schematic representation of the 3-element Windkessel model . . . 16
6 Sketch of the large cerebral arteries . . . 18
7 Lumped 0D-model of the cerebrovascular system . . . 20
8 0D-model of cerebrovascular system connected to the 0D-model of the head and neck vessels . . . 21
9 Sketch of arterial vessel segment with stenosis and 0D-model approach 25
10 Block diagram of the phenomenological-based autoregulation model . 26
11 Sigmoidal curve σ_j over error signal x for large cerebral arteries . . . 27
12 Baseline values for flow and pressure in the proximal arteries and the circle of Willis . . . 30
13 Response of state variables and the autoregulation mechanism to a sudden increase in arterial pressure P_a . . . 33
14 Recovery of the intracranial pressure after a sudden increase in aterial pressure . . . 35
15 Cerebrospinal fluid production and reabsorption after increase in arterial pressure . . . 35
16 Autoregulatory response over a range of arterial pressures . . . 36
17 New baseline flow and pressure distribution in the CoW for a patient with a 85 % stenosed right carotid artery . . . 39
18 Flow and pressure distribution in the CoW for a patient with a 85 % stenosed right carotid artery after the clamping of the right carotid artery . . . 40
19 Response of the state variables during the clamping of the right carotid artery for a patient with a stenosed right carotid artery . . . 41
20 New baseline flow and pressure distribution in the CoW for a patient with 85 % stenosed CAs and 75 % stenosed VAs . . . 42
21 Flow and pressure distribution in the CoW for a patient with 85 % stenosed CAs and 75 % stenosed VAs after the clamping of the right carotid artery . . . 43
22 Response of the state variables during the clamping of the right carotid artery for a patient with stenosed CAs and VAs . . . 44

23 New baseline flow and pressure distribution for a patient with stenosed CAs and VAs combined with missing PCoA and PCA,P1 46
24 Flow and pressure distribution after the clamping of the right carotid artery. Patient has stenosed CAs and VAs in combination with missing PCoA and PCA,P1 47
25 Response of the state variables during carotid clamping for a patient with stenosed CAs and VAs in combination with missing PCoA and PCA,P1 48

List of Tables

1 Mean values for length and radius for all large arteries of the head and neck [2] 19
2 Baseline values of hemodynamic quantities and model parameters for the 0D-model of the cerebral vasculature 31
3 Drop in blood flow relative to the normal baseline values for all six large cerebral arteries 49

Acronyms

ACA	Anterior cerebral artery
ATP	Adenosintriphosphat
BA	Basilar artery
CA	Carotid artery
CBF	Cerebral blood flow
CCA	Common carotid artery
CEA	Carotid endarterectomy
$CMRO_2$	Cerebral metabolic rate of oxygen
CO	Cardiac output
CoW	Circle of Willis
CSF	Cerebrospinal fluid
ECA	External carotid artery
EEG	Electroencephalography
ICA	Internal carotid artery
ICP	Intracranial pressure
MCA	Middle cerebral artery
PCA	Posterior cerebral artery
PCoA	Posterior communicating artery
RBC	Red blood cell
TCD	Transcranial Doppler
VA	Vertebral artery
VSM	Vascular smooth muscle
WK	Windkessel

1 Introduction

The cerebral vasculature is an elaborate system of arteries and veins that supplies the brain with oxygenated blood and nutrients and removes deoxygenated blood and waste from the brain back to the heart and lungs. The brain is very sensitive to changes in oxygen levels and therefore to changes in cerebral blood flow (CBF). A severe loss in blood flow (ischemia) leads to neurological symptoms within seconds. An oxygen deprivation for several minutes may even lead to irreversible damage to the brain functions [10]. The local cerebral autoregulation is an innate mechanism of the cerebral vasculature that allows to maintain a steady cerebral blood flow in the face of arterial blood pressure variations and to adapt the oxygen supply to the oxygen demand. The autoregulatory mechanism works at the level of the small arteries by altering the compliance and resistance of the vessel and thereby changing blood flow. These vessel properties are adapted through the vascular smooth muscle (VSM), which is located in the media of the vessel walls, via constriction and dilation of the vessel. The VSM is activated by the combined effects of multiple interacting mechanisms, including sensitivity to pressure, flow rate, metabolite levels, and neural signals.

Cardiovascular diseases are one of the top health problems in the western world and the number one cause of death in the United States. According to the American Heart Association, stroke is the second highest ranked cardiovascular disease after coronary heart disease. A stroke refers to the event in which some of the brain functions are lost, mostly due to inadequate oxygen supply to the brain tissue. Ischemia can either be caused by general hypoperfusion or by a blockage of the vessel via thrombosis or arterial embolism. One of the diseases leading to ischemic events is carotid stenosis. Plaque build up in the bifurcation of the carotid artery, caused by atherosclerosis, creates a local narrowing of the artery. The common practice in this event is to remove the plaque surgically via a carotid endarterectomy. In this procedure, the carotid artery is clamped, allowing the surgeon to open the diseased part of the vessel and to clean the inside of the vessel. During the course of the clamping, the blood flow through the carotid artery is completely stopped and redirected through the remaining arteries supplying the brain. This sudden loss in blood flow activates the cerebral autoregulation in an attempt to restore CBF. One of the main challenges of this procedure is to ensure sufficient flow to the brain and to avoid ischemia caused by the temporary clamping.

The objective of this work is to design and implement a reduced order computational model of the cerebral vasculature, including local autoregulatory control mechanisms. The proposed 0D-model is based on Poiseuille's Law and is able to reproduce reported literature values for average baseline flow and pressure in the cerebral vasculature. The large cerebral arteries, including the proximal arteries and the circle of Willis, are individually modeled via resistances. The small arteries, capillaries, and venous side are lumped together and modeled via Windkessel models. This model of the cerebral hemodynamics is complemented with a phenomenological-based autoregulation model, which accounts for changes in CBF by adapting the compliance and resistance of the small cerebral arteries. The 0D-model allows to simulate the transient behavior of the cerebral vasculature in response to a sudden change in hemodynamics. Of particular interest is the change in compliance and resistance of the small arteries induced by the local autoregulation. Representing the vessel's capacity to adjust its caliber to changes in hemodynamic is very important for many surgical procedures to ensure that the brain tissue is sufficiently perfused. The focus of this investigation is on the ability of the cerebrovasculature to compensate a loss in CBF for various degrees of stenosis severity.

Autoregulation models can generally be divided into two categories. The first group considers models attempting to describe the underlying physiology of the involved autoregulatory mechanisms. Currently the chemical mechanisms on the cellular level, leading to VSM activation are not fully understood. For this reason, these models tend to include a mathematical description of the physiology up to a certain point, usually before the cellular level, and then incorporate phenomenological-based lumped parameters to complete the mechanism chain between the trigger for autoregulation and the response of the VSM. *Carlson and Secomb* [5] [18] developed mathematical models that incorporated the individual contributions of myogenic, shear-dependent, and metabolic responses to the autoregulation of blood flow. *Van de Vosse et al.* [19] combined a mathematical model of the individual autoregulation mechanisms with neurovascular coupling. The blood flow regulation model was connected to a lumped parameter model of the posterior cerebral artery and its distal vessels. The second group of model allows to reproduce experimental data rather than describing the underlying physiology. Model parameters are fit to experimental measurements like blood pressure and cerebral blood flow velocity. These models are often able to reproduce well the physiological response of the cerebrovascular. *Ursino and Lodi* have developed phenomenological-based autoregulation models in

combination with lumped parameter models of the cerebral vasculature. In [20], a simple mathematical model to simulate the interaction between intracranial pressure, cerebral blood volume, and autoregulation is presented. This model is extended in [14] to simulate vasospasm in one of the large cerebral arteries.
Models of the cerebral vasculature can be categorized according to the formulation of the governing fluid mechanics equations. *Moorhead et al.* [17] used a 0D approach based on Poiseuille flow to model blood flow in the CoW. This model was combined with a physiological-based autoregulation model to simulate the metabolic response. *Alastruey et al.* [2] proposed a 1D approach to simulate the blood flow in the circle of Willis. This model is able to capture the main features of pulse wave propagation in the cerebral arteries and was used to investigate the impact of anatomical variations on cerebral hemodynamics. *Moore et al.* [16] presented a three-dimensional model based MRI data combined with a autoregulation model, accounting for the metabolic-controlled autoregulation mechanism. This model was used to simulate oxygen delivery to the brain in response to flow changes caused by a stenosis.

This work is organized as follows. In Section 2, background on cerebral autoregulation and vasculature is provided. Subsequently, the basic steps of the carotid endarterectomy surgical procedure are outlined. In Section 3, the formulations of the lumped-parameter cerebrovascular model and the autoregulation model are introduced. Section 4 shows the results of test cases verifying the performance of the autoregulation model. Following, the clamping stage of a carotid endarterectomy procedure is simulated for various patient scenarios. Section 5 discusses the results in the light of the model assumptions. The most important results of the investigation and an outlook for further studies are summarized in Section 6.

2 Physiology

2.1 Cerebral vasculature

2.1.1 Circle of Willis

The cerebral circulation receives approximately $15-20\,\%$ of the cardiac output. The two internal carotid arteries ($80\,\%$ of CBF) and the two vertebral arteries ($20\,\%$ of CBF) supply the brain with blood through the circle of Willis (CoW). The CoW is a ring-like structure of blood vessels located in the base of the brain beneath the hypothalamus, see Figure 1. This formation serves as a backup system for the blood supply. In the case of a blocked artery, this network of collateral arteries allows to compensate the blood flow. The two vertebral arteries come together intracranially in the basilar artery. At the CoW, each of the two internal carotid arteries branches into the middle and anterior cerebral arteries, supplying the the frontal, temporal, and parietal regions of the brain with blood. The basilar artery splits into the right and left posterior cerebral arteries, supplying blood to the occipital lobe, cerebellum and the brain stem. The posterior and anterior cerebral arteries are connected via the posterior communicating arteries and the two anterior cerebral arteries via the anterior communicating artery. There is a considerable high number of variations in the anatomy of the circle of Willis. Studies have shown that in approximately $50\,\%$ of healthy brains the CoW is at least missing an artery or contains an underdeveloped artery [3]. In dysfunctional brains this number is even higher. These variations from the classical anatomy may lead to limited blood flow to the cerebral arterioles and cause an increased risk of stroke.

2.1.2 The Monro-Kellie hypothesis

The Monro-Kellie hypothesis states that the cranial volume inside the skull is incompressible. The cranial volume consists of three components: cerebral blood volume, cerebrospinal fluid volume, and brain tissue. The volume of these components is always in a state of equilibrium, defining the intracranial pressure. An increase of one of the volumes must be compensated by a decrease of one of the other volumes in order to keep the intracranial pressure constant.

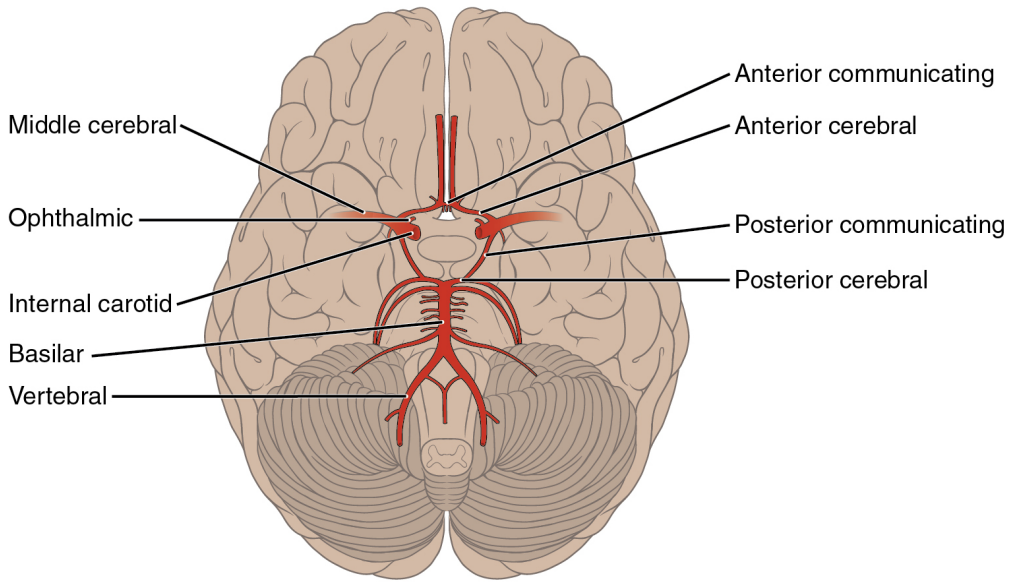

Figure 1: Inferior view of the cerebral arteries forming the circle of Willis [1]

2.1.3 Cerebrospinal fluid

The cerebrospinal fluid (CSF) is a clear and colorless fluid found in the brain and the spine. CSF is produced from blood by the choroid plexus in the ventricles of the brain and is reabsorbed at the dural venous sinuses back in the venous circulation. In Addition to providing a cushion for the brain tissue, the CSF is responsible for the transport of metabolic waste products, chemicals, antibodies etc. away from the brain and spinal-cord tissue into the bloodstream. The brain produces roughly 500 ml of cerebrospinal fluid per day. The available cranial volume allows only $100 - 160$ ml to be present at any time. Thus the CSF turns over about 3.7 times a day.

[1] Source: http://cnx.org/contents/1aa6075b-8678-43f0-891d-cff6252fb2eb@3/Circulatory_Pathways

2.2 Cerebral autoregulation

The term cerebral autoregulation incorporates several mechanisms that activate the vascular smooth muscle simultaneously through various channels. The activation of VSM produces a nonlinear autoregulatory response. In the following, the most dominant mechanisms of the cerebral autoregulation are presented.

Myogenic response: The myogenic response refers to the relaxation/constriction of the arterial vessels due to variations in perfusion pressure. An increase in perfusion pressure leads to an increase in flow and to a stretching of the arterial vessels (passive tension). At a certain tension threshold, the smooth muscle of the blood vessels reacts to the stretching of the muscle by opening ion channels, which causes the muscle to depolarize, leading to muscle contraction (active tension). The decrease in vessel diameter results in a larger resistance and a subsequent decrease in flow. The myogenic response is a feedback mechanism that tries to minimize the error between the current and a baseline level of wall tension.

The myogenic response of arterioles is triphasic. At low pressures, arterioles dilate passively with increasing pressure. The vessel wall tension is not enough to activate the myogenic response. With increasing pressures from 50 to 150 mmHg, the active myogenic response is activated to change the diameter. At high pressures above 150 mmHg, the myogenic response is exhausted and the vessel remains dilated despite the generation of maximal VSM tone. The capacity to further change the vessel diameter is exhausted, any additional increase in pressure leads to a direct dilation of the vessel.

Shear-dependent response: The shear-dependent response is activated by changes in wall-shear stress in the endothelium. The endothelium is single layer of cells lining the blood vessel, separating the lumen from the wall tissue (see Figure 2). Following an increased in shear stress, nitric oxide (NO) is released by the endothelium, which results in vasodilation. The wall-shear stress is inversely proportional to the third power of the vessel radius. Thus, by increasing the vessel radius the wall-shear stress decreases.

The shear-dependent and myogenic response work in opposite directions on the vascular smooth muscle. For example, an increase in perfusion pressure leads to an increase in wall tension and wall-shear stress. While the myogenic response aims at reducing the wall tension by constricting the vessel, the shear-dependent response attempts to reduce the wall-shear stress by dilating the vessel.

Metabolic response: There are several metabolites that control the metabolic response, two of the most important representatives are O_2 and CO_2. The metabolic response is a feedback mechanism. A difference between the O_2 demand and saturation in the tissue causes an upstream reaction in the small arteries. The VSM changes the vessel properties in order to adjust the blood flow, thereby minimizing the difference between demand and supply.

Besides carrying oxygen in the blood, red blood cells (RBCs) also act as oxygen sensors. RBCs respond to oxygen levels by releasing Adenosintriphosphat (ATP) at a rate that depends on their oxyhemoglobin saturation level. This ATP release initiates a conducted response that travels upstream and triggers vaso-dilation /constriction.

Neurovascular coupling: The neurovascular coupling refers to the adaptation of the arteriolar resistance and compliance in response to changes in brain activity. A change in neural activity leads to a direct change in the cerebral metabolic rate of oxygen consumption and in the vascular smooth muscle tone via sympathetic innervation. This instantaneous control of the VSM is a feedforward mechanism. The feedforward mechanism is an anticipative response that tries to counter an expected change in metabolic demand before a difference between demand and supply actually arises. While the change in vessel caliber is fast, it is also inaccurate. In comparison, the feedback mechanism only reacts to an error signal, minimizing it precisely. The combination of feedback and feedforward mechanisms is therefore needed to provide a fast and accurate autoregulatory response.

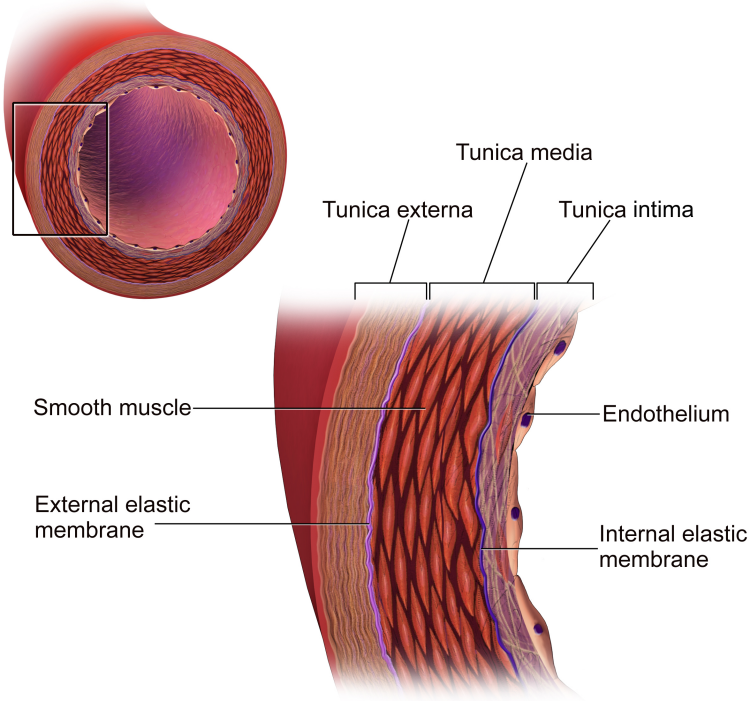

Figure 2: Structure of the arterial vessel wall [2]

Smooth muscle can be found in many organs in the body such as the stomach, bladder, iris, and blood vessels. The vascular smooth muscle (VSM) is located in the media of the vessel (see Figure 2). The VSM is organized in two groups of cells, multi-unit and unitary cells. The multi-unit muscle cells are innervated by sympathetic nerves and controlled as a unit through the central nervous system. The unitary muscle cells on the other hand are individual cells that are connected and activated through gap junctions, which mediate ionic current and action potentials. In comparison to skeletal muscle cells, smooth muscle cells can produce force over a wide range of muscle cell lengths and can sustain a constant force over a long time period. This ability to stretch and maintain contractility is important for blood vessels. The activation of the smooth muscle cells is a calcium-driven mechanism.

[2]Source: http://en.wikiversity.org/wiki/Blausen_gallery_2014#mediaviewer/File:Blausen_0055_ArteryWallStructure.png

2.3 Carotid stenosis and endarterectomy

Carotid stenosis is one of the most widely spread cerebral vasculature diseases and one of the main causes of stroke. The term stenosis refers to a narrowing of the artery. In most of the cases, the stenosis in the carotid artery is located at the bifurcation of the internal and external carotid artery, see Figure 3. This narrowing is usually caused by a buildup of plaque, consisting of fatty substances and cholesterol deposits, a process known as atherosclerosis. Atherosclerosis also causes arteries to become stiffer. There are several ways in which carotid stenosis increases the risk of stroke. First, the plaque deposits can grow larger and larger, severely narrowing the artery and reducing perfusion to the brain. This can eventually lead to a completely occluded artery. Second, the plaque buildup changes the characteristics of the surface of the vessel wall. The rough structure of the plaque increases the possibility of clot formation and blocking of the artery. Plaque deposits can also rupture and break away, traveling downstream to get stuck in a smaller artery and block blood flow to the brain.

Carotid endarterectomy (CEA) is a surgical procedure performed on patients with a severely stenosed carotid artery to reduce the risk of stroke and improve brain perfusion. According to the guidelines of the National Institute for Health and Clinical Excellence, symptomatic patients with a $50 - 99\,\%$ stenosis should have a CEA as soon as possible. A patient is considered symptomatic when transient ischemic attacks (TIA) occur. TIAs are events where the blood flow to parts of the brain is temporarily stopped, mimicking stroke-like symptoms. Unlike in stroke, the blockage disappears after a short time without leaving permanent damage. The procedure is recommended for patients who do not show symptoms but have a blockage greater than $60\,\%$.

The surgical procedure of a carotid endarterectomy consists of several steps, which are outlined in the following. First, a skin incision is made in the neck where the carotid artery is located. Next, the ICA and ECA and are completely occluded with micro-clamps distal of the narrowing to stop the blood flow. The CCA is subsequently clamped proximal to the plaque. The surgeon makes an incision, starting in the CCA and moving distally along the ICA until the end of the plaque is visible. The plaque buildup is physically peeled out and removed, see Figure 4 (left). The artery is then closed with tiny sutures and the clamps removed to restore blood flow. The procedure can be performed under local or general anaesthesia. According to

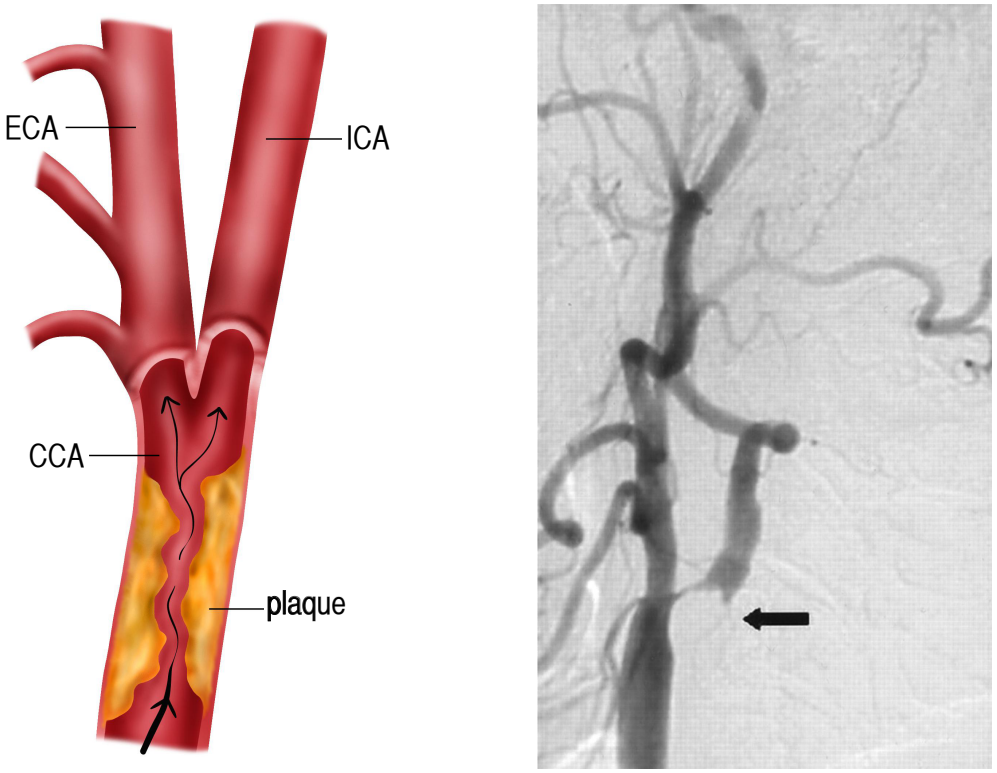

Figure 3: Left: Plaque buildup in the common carotid artery [3]. Right: Digital subtraction angiography (DSA) of severe stenosis in the ICA (black arrow) [4]

[12], cerebral autoregulation remains intact during both local and general anaesthesia.

One of the possible complications during the procedure is ischemia. The sudden stop in blood flow through the clamped carotid artery may cause an oxygen deficiency in the brain tissue. To ensure sufficient brain perfusion during the procedure, some surgeons insert a temporary shunt in the carotid artery (Figure 4 (right)). The clamped region is bypassed by a graft, connecting the common and the internal carotid arteries. The use of a shunt during the procedure is however highly controversial, since it may cause further complications such as intimal tears or short dissections [4]. There are several methods to monitor cerebral blood flow during the procedure to determine the need for selective shunting.

[3]Source: https://neuro4students.wordpress.com/pathophysiology/
[4]Source: http://stroke.ahajournals.org/content/34/3/660.figures-only

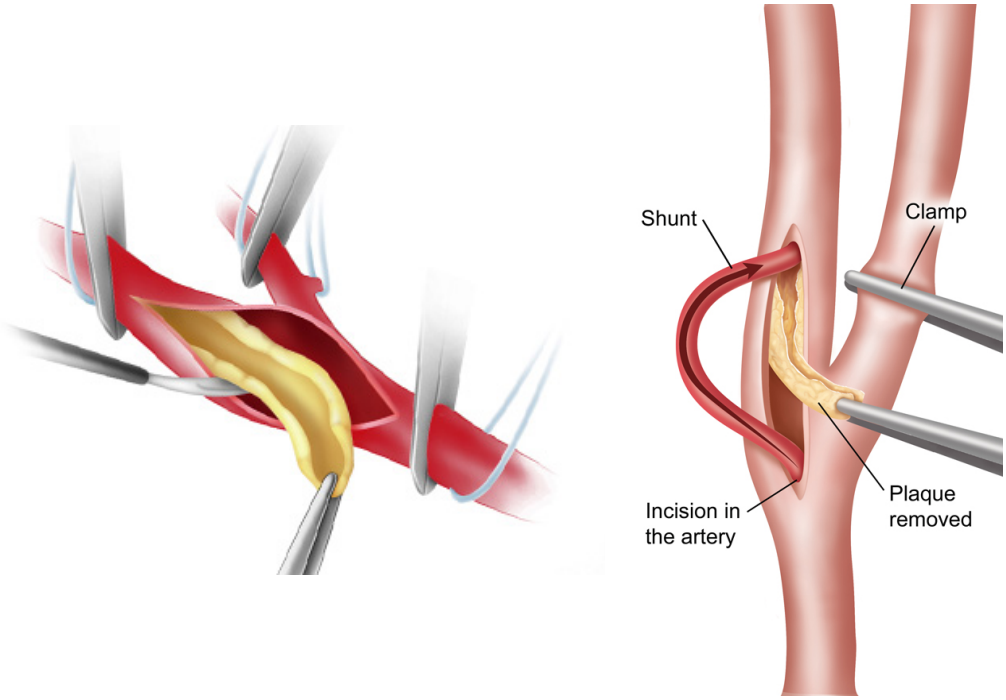

Figure 4: Left: Removal of plaque during carotid endarterectomy [5] . Right: Use of a shunt to bypass blood from the CCA to the ICA during carotid endarterectomy [6]

Transcranial Doppler (TCD): The transcranial Doppler method measures non-invasively the blood velocities in the large cerebral arteries via ultrasonic techniques. With the help of this method, changes in brain perfusion as well as the appearance of emboli during the procedure can be detected.

Electroencephalography (EEG): EEG refers to the recording of electrical activity of the brain. Changes in the measured ionic current flows may indicate regions with insufficient blood supply during the operation. Unfortunately, the method can not differentiate between ischemia caused by low perfusion or embolization. In the latter case, the insertion of a shunt would not reverse the ischemic condition [4].

Patient interrogation: The patient is under regional anesthesia, allowing the surgeon to periodically communicate with the patient. In the case of sudden unresponsiveness, a shunt is inserted to improve perfusion. According to [4], this method leads to an overestimation of the need for a shunt. These levels

[5]Source: http://www.michiganstrokenetwork.com/Treatment/Procedures/v/Carotid_Endarterectomy/patients.aspx

[6]Source: http://www.hopkinsmedicine.org/healthlibrary/test_procedures/cardiovascular/carotid_endarterectomy_carotid_angioplasty_with_stenting_92,p08293/

of relative ischemia will not damage the brain cells and brain functions will be restored when perfusion returns to normal levels, unless the loss of perfusion is prolonged.

Carotid back-pressure: In this method, the pressure in the ICA is measured after clamping the CCA and ECA. The measured pressure indicates the degree of collateral flow available. According to [4], a back-pressure below 25 mmHg is the common criteria for inserting a shunt. Again, this criteria often leads to an overuse of shunts.

An alternative surgical procedure to the carotid endarterectomy is the endovascular angioplasty with stenting. In this procedure, a catheter is inserted into the femoral artery and guided through the aorta to the carotid artery. At the location of the stenosis, a balloon is inflated, which opens up the vessel. Afterwards, a wire-mesh stent is inserted to prevent the vessel from narrowing again and to protect the brain from embolization of plaque material. However, the risk of a stroke or heart failure after the stenting is significantly higher than with the CEA.

3 Methods

In this chapter, a complete list of the equations describing the computational model of the cerebrovascular is presented. In the first part, the equations describing the cerebral flow are shown and in the second part the autoregulation model is introduced.

3.1 Modeling cerebral blood flow

3.1.1 Poiseuille's Law

Poiseuille's Law describes the pressure drop in an incompressible, laminar flow going through a straight cylindrical tube. The pressure drop ΔP through a tube can be described as

$$\Delta P = R \cdot Q, \tag{1}$$

where R is the resistance and Q the blood flow . This relationship is only valid for axially symmetric and fully developed flow. The resistance accounts for the viscous losses along the tube and is calculated as

$$R = \frac{8\mu L}{\pi r^4}, \tag{2}$$

where μ is the dynamic viscosity of the blood, L and r are the vessel length and radius, respectively. Due to the strong dependency of the resistance to the radius, small changes in r lead to large changes in R.

One of the most used models to simulate blood flow in the arterial system is the 3-element Windkessel. Figure 5 shows the electrical analog of the 3-element Windkessel. This model consists of a proximal resistance R_p, accounting for the viscous losses in the proximal vessels and a distal resistance R_d, modeling the viscous losses in the peripheral vasculature. The capacitor C models the elastic behavior of the vascular bed. During systole, the vessels extend due to the rise in blood pressure, increasing the blood volume stored in the vessels. During diastole, the blood pressure drops and the vessels contract again, releasing the stored blood volume. The compliance of the vessels can be modeled with a capacitor

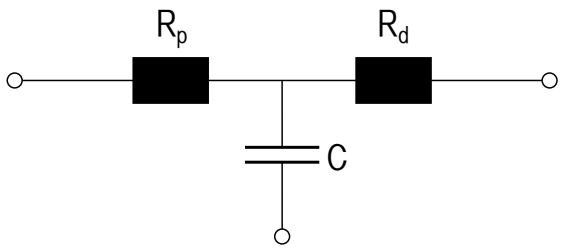

Figure 5: Schematic representation of the 3-element Windkessel model

$$C = \frac{\Delta V}{\Delta P_{trans}}. \tag{3}$$

ΔV is the change in blood volume and ΔP_{trans} the change in transmural pressure. The transmural pressure is defined as the difference between the inside and outside pressure of the tube. In the cerebral vasculature, the outside pressure is defined as the intracranial pressure.

3.1.2 0D-model of the head and neck vessels

In order to investigate changes in CBF caused by carotid stenosis, variations in the anatomy of the CoW and the clamping of the carotid artery during an endarterectomy, a model of the head and neck vessels must be constructed. In the first step, the proximal arteries and the circle of Willis are modeled with a 0D-model approach according to Poiseuille's Law.

Figure 6 (left) shows a sketch of the modeled vasculature and Figure 6 (right) illustrates an electrical analog of the system using resistors. According to Poiseuille's Law, each arterial segment is modeled via a resistance, see Eq. (2). For simplicity, the compliance of the large arteries is neglected. The calculation of the resistance of each vessel is based on data on length and radius as reported in [2] and shown in Table 1. These values represent average measurements for a healthy young adult.

The resistances are fitted in order to reproduce an average baseline distribution of flow and pressure. In the following, several flow and pressure assumptions are made. First, the right and left side of the circle of Willis are assumed to have symmetrical pressure and flow values. According to [2], the flow is distributed as follows: 15% of the cardiac output goes to the head, 5% flow to each arm, and the remaining 75% perfuse the lower body through the descending thoracic aorta. In normal baseline conditions, the perfusion of the large cerebral arteries does not rely on the posterior and anterior communicating arteries. The flow through the communication arteries is two orders of magnitude smaller than the flow through the large cerebral arteries. According to [6], the flow ratio between carotid and vertebral arteries is 85% : 15%. The flow ratio between common carotid artery and internal carotid artery is assigned according to Doppler velocity measurements from [11]. The average velocity ratio for a young and healthy subject results to $\frac{V_{ICA}}{V_{CCA}} = 1.05$, which can be converted to a flow ratio with the mean vessel radius of Table 1.

3.1.3 0D-model of cerebrovascular system

In this section, a lumped parameter model for the cerebrovascular system is presented. This model is based on the work of *Ursino et al.* [14] [20]. It includes the small and large arteries, the capillaries, the venous system, the cerebrospinal fluid circulation, and the intracranial Pressure.

Figure 7 shows a sketch of the mechanical analog of the circuit. The total cerebral blood flow q_a is the sum of the blood flow through the right and left internal carotid arteries and the basilar artery. In this model, all inflows are lumped together into a single vessel, entering the skull with systemic arterial pressure P_a. The large arteries of the circle of Willis are represented by the resistance R_{la}. The small arteries distal of the circle of Willis (pial arteries) are modeled with a 3-element Windkessel, consisting of the pial artery resistance R_{pa} and compliance C_{pa}. The arterioles merge into the capillaries at capillary pressure P_c. The venous circulation is also modeled with a 3-element Windkessel, consisting of the proximal venous resistance R_{pv}, the intracranial venous compliance C_{vi}, and the terminal venous resistance R_{vs}. P_v is the venous pressure and P_{vs} is the pressure at the dural sinuses. This model also incorporates the cerebrospinal fluid (CSF), surrounding the arteries, veins, and brain tissue in the skull. CSF is produced at the capillaries through the CSF formation resistance R_f and reabsorbed at the dural sinuses through the CSF outflow resistance R_o. The intracranial pressure P_{ic} is determined by the nonlinear craniospinal storage

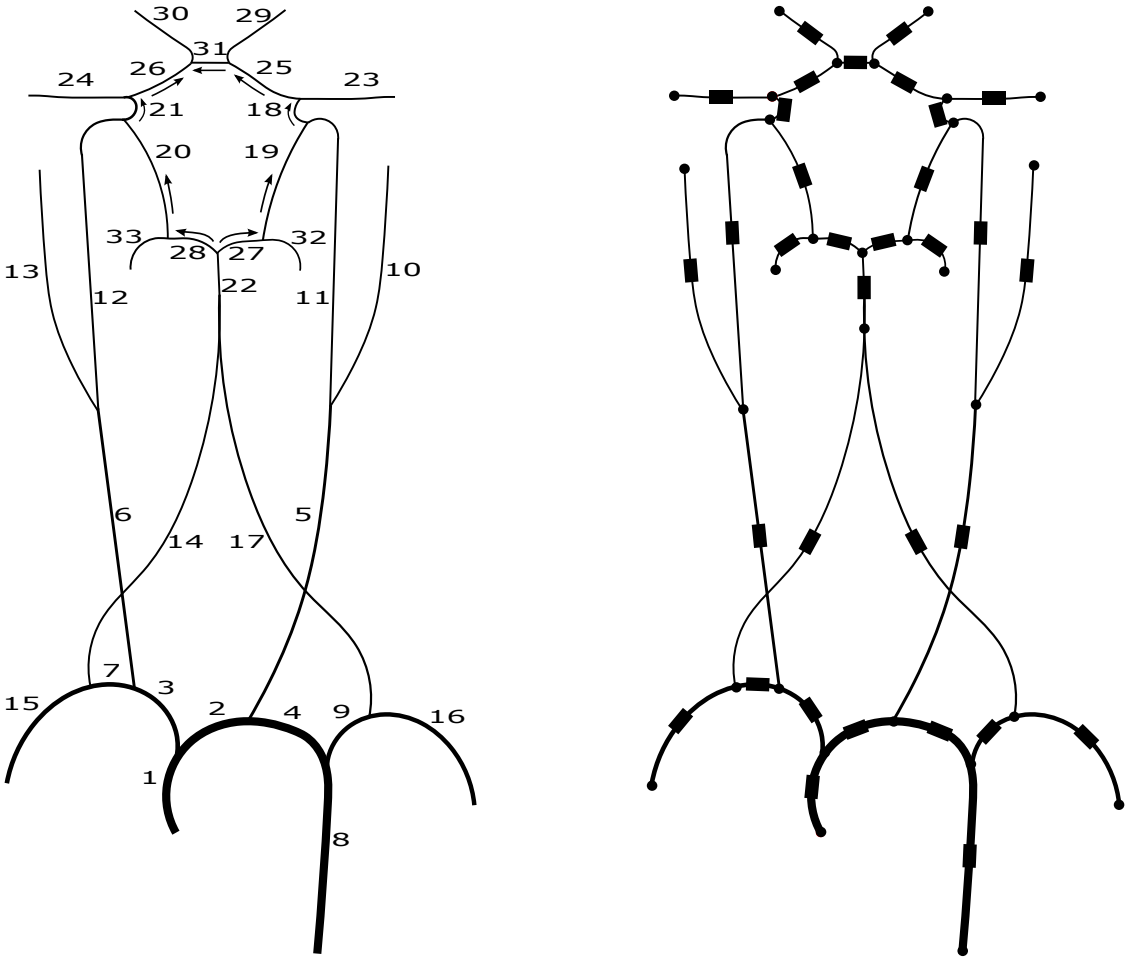

Figure 6: Left: Sketch of the anatomy of the head and neck vessels. The arrows symbolize the flow direction under normal baseline condition in the CoW. The numbers refer to segment name, see Table 1. Right: Electrical analog of the head and neck vessels

Arterial segment	Length [cm]	Radius [cm]
1. Ascending aorta	4.0	1.2
2. Aortic arch I	2.0	1.120
3. Brachiocephalic	3.4	0.590
4. Aortic arch II	3.9	1.070
5. L. common carotid	20.8	0.254
6. R. common carotid	17.7	0.244
7. R. subclavian	3.4	0.423
8. Thoracic aorta	15.6	0.999
9. L. subclavian	3.4	0.423
10. L. ext. carotid	17.7	0.150
11. L. int. carotid I	17.7	0.20
12. R. int. carotid I	17.7	0.20
13. R. ext. carotid	17.7	0.150
14. R. vertebral	14.8	0.127
15. R. brachial	42.2	0.403
16. L. brachial	42.2	0.403
17. L. vertebral	14.8	0.127
18. L. int. carotid II	0.5	0.200
19. L. PCoA	1.5	0.073
20. R. PCoA	1.5	0.073
21. R. int. carotid II	0.5	0.200
22. Basilar	2.9	0.160
23. L. MCA	5.3	0.143
24. R. MCA	5.3	0.143
25. L. ACA, A1	1.2	0.117
26. R. ACA, A1	1.2	0.117
27. L. PCA, P1	0.5	0.107
28. R. PCA, P1	0.5	0.107
29. L. ACA, A2	4.3	0.125
30. R. ACA, A2	4.3	0.125
31. ACoA	0.3	0.074
32. L. PCA, P2	4.63	0.105
33. R. PCA, P2	4.63	0.105

Table 1: Mean values for length and radius for all large arteries of the head and neck [2]

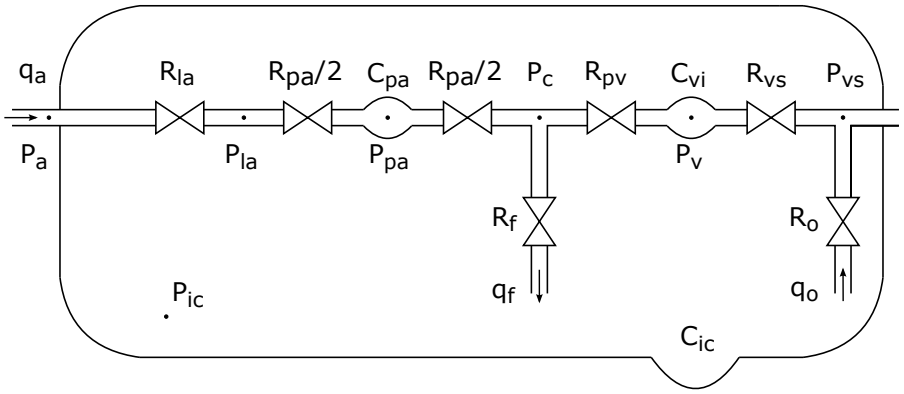

Figure 7: 0D-model of the cerebrovascular system. All large cerebral arteries are lumped together into a single branch.

capacity C_{ic}. The craniospinal volume is assumed to be constant (Monro-Kellie hypothesis, Section 2.1), balancing CSF inflow and outflow and change in arterial and venous blood volume.
In this model, the compliance and resistance of the pial arteries C_{pa} and R_{pa} are actively regulated by the autoregulation mechanism (see Section 3.2). The remaining parameters of the model are assumed to be constant throughout the simulations.

Next, the 0D-model of the head and neck vessels is connected to the 0D-model of the cerebrovascular system. This is illustrated in Figure 8, where all large cerebral branches are modeled individually, each with a 3-element Windkessel. This is achieved by parallelizing the pial resistances and compliances. The left side of the model, representing the large arteries, is replaced by the 0D-model of the head and neck vessels.

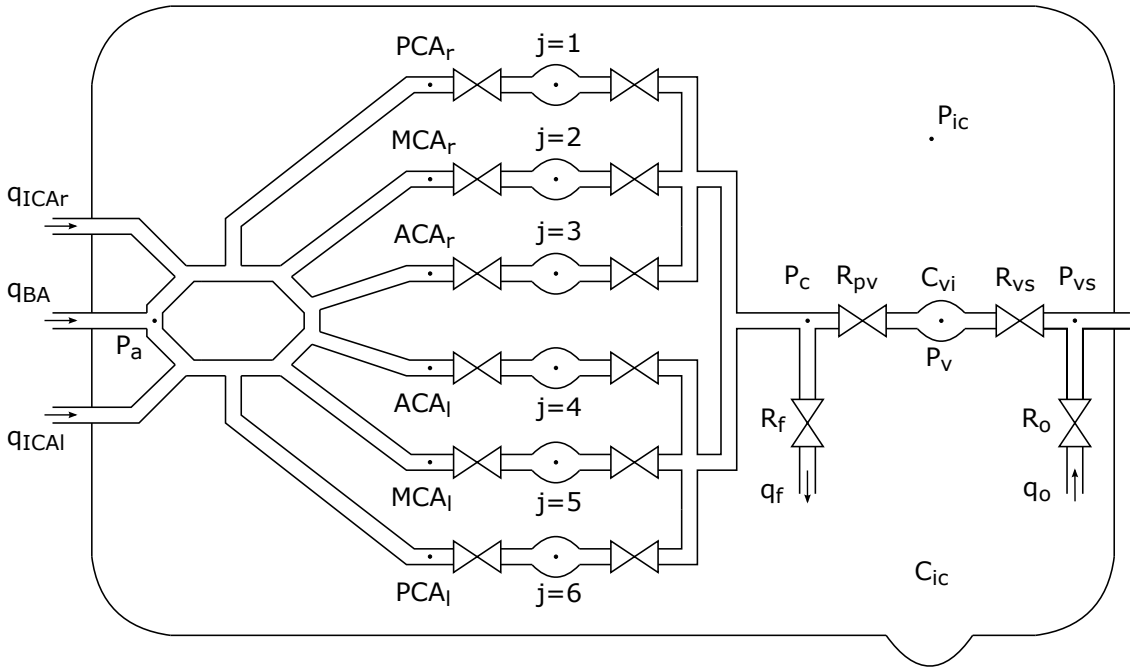

Figure 8: 0D-model of cerebrovascular system connected to the 0D-model of the head and neck vessels. Each cerebral artery is modeled individually.

In the following, the equations describing the cerebrovascular system are derived. The relationship between the values of the single branch and the parallelized model for pial resistance and compliance is defined as:

$$\frac{1}{R_{pa,Tot}} = \sum_{j=1}^{6} \frac{1}{R_{pa,j}} \tag{4}$$

$$C_{pa,Tot} = \sum_{j=1}^{6} C_{pa,j}, \tag{5}$$

with

$$\frac{1}{R_{pa,j}} = k_{p,j} \cdot \frac{1}{R_{pa,Tot}} \tag{6}$$

$$C_{pa,j} = k_{p,j} \cdot C_{pa,Tot} \tag{7}$$

$$\sum_{j=1}^{6} k_{p,j} = 1. \tag{8}$$

$k_{p,j}$ is a weighting factor, representing the relative impact of the jth cerebral artery to the total pial resistance and compliance. $k_{p,j}$ is defined as the fraction of blood

flow in the jth branch relative to the total CBF representing baseline conditions. Applying the conservation of mass at the level of the pial arteries yields

$$\frac{\mathrm{d}V_{pa,j}}{\mathrm{d}t} = \frac{P_{la,j} - P_{pa,j}}{R_{pa,j}/2} - \frac{P_{pa,j} - P_c}{R_{pa,j}/2} \qquad j = 1, ..., 6 \tag{9}$$

where $V_{pa,j}$ is the blood volume of the pial artery. At the capillary level, all branches merge again into one venous branch, leading to

$$\sum_{j=1}^{6} \frac{P_{pa,j} - P_c}{R_{pa,j}/2} = \frac{P_c - P_{ic}}{R_f} + \frac{P_c - P_v}{R_{pv}}. \tag{10}$$

Equilibrium with the venous compliance results in:

$$C_{vi}\left(\frac{\mathrm{d}P_v}{\mathrm{d}t} - \frac{\mathrm{d}P_{ic}}{\mathrm{d}t}\right) = \frac{P_c - P_v}{R_{pv}} - \frac{P_v - P_{vs}}{R_{vs}}. \tag{11}$$

The venous compliance changes passively with the transmural pressure. In order to derive a simple expression for the venous compliance, a monoexponential pressure volume relationship is assumed:

$$C_{vi} = \frac{1}{k_{ven}\left(P_v - P_{ic} - P_{v1}\right)}, \tag{12}$$

with k_{ven} being a constant parameter defining the slope of the monoexponential curve. P_{v1} represents the pressure at which the terminal veins collapse (Starling resistor hypothesis). When the transmural pressure approaches this value, the compliance increases significantly. The narrowing of the terminal veins leads to an increase in resistance, modeled with the following expression

$$R_{vs} = R'_{vs} \cdot \frac{P_v - P_{vs}}{P_v - P_{ic}}, \tag{13}$$

where R'_{vs} is the terminal venous resistance for collapsed veins ($P_{vs} = P_{ic}$). Based on the consistency of the intracranial volume, the following equations can be derived

$$C_{ic} \cdot \frac{\mathrm{d}P_{ic}}{\mathrm{d}t} = \sum_{j=1}^{6} \frac{\mathrm{d}V_{pa,j}}{\mathrm{d}t} + C_{vi} \cdot \left(\frac{\mathrm{d}P_v}{\mathrm{d}t} - \frac{\mathrm{d}P_{ic}}{\mathrm{d}t} \right) + \frac{P_c - P_{ic}}{R_f} - \frac{P_{ic} - P_{vs}}{R_o}. \tag{14}$$

The first term on the right side of the equation represents the arterial volume change. The second term accounts for the venous volume change. The last two terms are the cerebrospinal fluid production and reabsorption, which are passive mechanisms driven by the capillary and venous sinus transmural pressure respectively. In order to calculate the intracranial compliance, a monoexponential pressure-volume relationship is assumed as follows

$$C_{ic} = \frac{1}{k_E P_{ic}}, \tag{15}$$

where k_E is the elastance coefficient relating the intracranial compliance inversely proportional to the intracranial pressure. The pial artery volume can be calculated through the pial compliance as follows

$$V_{pa,j} = C_{pa,j} \cdot \left(P_{pa,j} - P_{ic} \right), \qquad j = 1, ..., 6. \tag{16}$$

By differentiating Eq. (16) one obtains

$$\frac{\mathrm{d}V_{pa,j}}{\mathrm{d}t} = C_{pa,j} \cdot \left(\frac{\mathrm{d}P_{pa,j}}{\mathrm{d}t} - \frac{\mathrm{d}P_{ic}}{\mathrm{d}t} \right) + \frac{\mathrm{d}C_{pa,j}}{\mathrm{d}t} \cdot \left(P_{pa,j} - P_{ic} \right), \qquad j = 1, ..., 6. \tag{17}$$

The first term on the right hand side represents the passive arterial volume change caused by the change in transmural pressure. The second term is the change in arterial volume based on the change in arterial compliance. The arterial compliance is actively controlled by the autoregulation, see Section 3.2. The pial resistance R_{pa} is directly related to the pial compliance C_{pa} through geometrical considerations. According to Poiseuille's Law,

$$R_{pa,j} = \frac{R_{pa0,j} \cdot r_{pa0,j}^4}{r_{pa,j}^4}, \qquad j = 1, ..., 6 \tag{18}$$

where $R_{pa0,j}$ and $r_{pa0,j}$ are the pial resistance and inner radius under baseline con-

ditions. Considering a cylindrical vessel, the volume is proportional to the second power of the radius, $V_{pa} \propto r_{pa}^2$. Inserting this relationship into Eq. (18) results in:

$$R_{pa,j} = \frac{R_{pa0,j} \cdot V_{pa0,j}^2}{V_{pa,j}^2}, \qquad j = 1, ..., 6. \tag{19}$$

The pial volume is directly connected to the pial compliance, see Eq. (16). The flow in the large cerebral arteries and at the tissue level can be calculated using the following equations

$$q_{a,j} = \frac{P_{la,j} - P_{pa,j}}{R_{pa,j}/2}, \qquad j = 1, ..., 6 \tag{20}$$

$$q_{tiss,j} = \frac{P_{pa,j} - P_c}{R_{pa,j}/2}, \qquad j = 1, ..., 6. \tag{21}$$

3.1.4 Modeling stenosis

The plaque buildup, seen in arterial stenosis, forms a rough and uneven surface, decreasing the effective diameter of the vessel. In a 0D-representation of the vessel, a stenosis can be modeled with an ad-hoc resistance. For the calculation of the resistance the vessel is divided into two segments, a stenosed part and a stenosis-free part. For simplicity, the radius of the lumen in the stenosed part is assumed to be a constant value along the length of the stenosis. This constant value represents an average radius of the stenotic lumen. Figure 9 shows an idealized geometry of a stenosis. The effective resistance of the stenosed vessel can be calculated as follows

$$R_s = \frac{8\mu}{\pi r_0^4}(l_0 - l_s) + \frac{8\mu}{\pi r_s^4} l_s. \tag{22}$$

This corresponds to two resistances in series. r_0 and l_0 represent the resistance and length of the healthy part of the vessel, r_s and l_s the resistance and length of the stenosed part of the vessel.

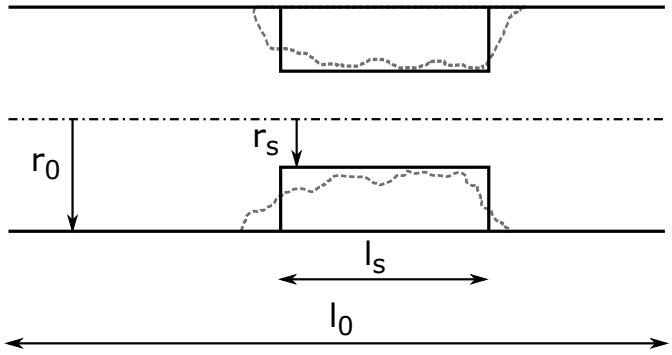

Figure 9: Sketch of arterial vessel segment with stenosis and 0D-model approach

3.2 Autoregulation model

The implemented autoregulation model is based on the work of *Ursino et al.* [20]. The basis of this model is a phenomenological-based observation of all autoregulatory feedback mechanisms lumped together into one response. This model does not distinguish between the individual feedback mechanisms presented in Section 2.2. Figure 10 shows the block diagram of the autoregulation model. The autoregulation mechanism is triggered by a difference between the flow demand of the brain tissue and the actual flow at the tissue level. In this work, the tissue demand is set to the initial baseline flow value. The model reacts to a deviation in flow by changing the pial compliance. The first block represents a gain, which amplifies the error signal. A lower value for this parameter can be used to simulate diseases which impair local autoregulation. The second block illustrates the static sigmoidal relationship between the error signal and compliance. The last block accounts for the dynamic behavior of the autoregulation. Here, this element is a low-pass filter. This model of the autoregulation mechanism represents a P-controller, which produces an output value proportional to the current error signal.

The autoregulation model is applied to all six cerebral arteries, $j = 1, ..., 6$. The block diagram can be described with the following differential equation

$$\frac{\mathrm{d}C_{pa,j}}{\mathrm{d}t} = \frac{1}{\tau} \cdot \left[-C_{pa,j} + \sigma_j \left(G \cdot x_j\right)\right], \tag{23}$$

with the time constant τ representing the time of the autoregulatory response. The error signal is defined as normalized difference between the flow at the tissue level and the baseline flow value

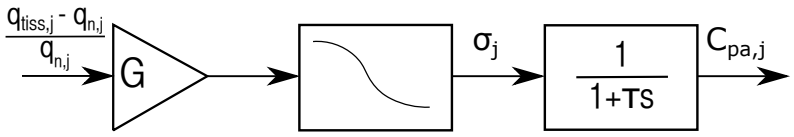

Figure 10: Block diagram of the phenomenological-based autoregulation model

$$x_j = \frac{q_{tiss,j} - q_{0,j}}{q_{0,j}}. \tag{24}$$

The sigmoidal relationship can be written as

$$\sigma_j\left(G \cdot x_j\right) = \frac{\left(C_{pa\,0,j} + \Delta C_{pa,j}/2\right) + \left(C_{pa\,0,j} - \Delta C_{pa,j}/2\right) \cdot \exp\left(G \cdot x_j / k_{\sigma,j}\right)}{1 + \exp\left(G \cdot x_j / k_{\sigma,j}\right)}. \tag{25}$$

This equation maps the current error signal to a corresponding value for the compliance. $C_{pa\,0,j}$ represents the baseline compliance, $\Delta C_{pa,j}$ the amplitude of the sigmoidal curve, G the gain, and $k_{\sigma,j}$ the slope of the sigmoidal curve. $\Delta C_{pa,j}$ can be calculated as follows

$$\begin{cases} \text{if} \quad x_j <= 0: \quad \Delta C_{pa,j} = \Delta C_{pa\,max,j}; \\ \text{if} \quad x_j > 0: \quad\;\; \Delta C_{pa,j} = \Delta C_{pa\,min,j}, \end{cases} \tag{26}$$

which takes under consideration that the vessel's ability to change compliance is not symmetrical. The increase in blood volume caused by vasodilation is higher than the decrease in blood volume caused by vasoconstriction. $k_{\sigma,j}$ is defined as

$$k_{\sigma,j} = \Delta C_{pa,j}/16\, C_{pa\,0,j}. \tag{27}$$

The expression for $k_{\sigma,j}$ has been adapted from the original relationship stated in [20]. The autoregulation model was originally designed for a lumped 1-branch circuit model, see Figure 7. The value of k_σ sets the central slope of the sigmoidal curve at the error-signal $x = 0$ to $-G$. Due to the nonlinear nature of Eq. (25), the autoregulation response cannot simply be parallelized for our model (Figure 8). In order to yield the same autoregulatory response after parallelizing as the original model, the expression for $k_{\sigma,j}$ was adapted by multiplying the denominator by a

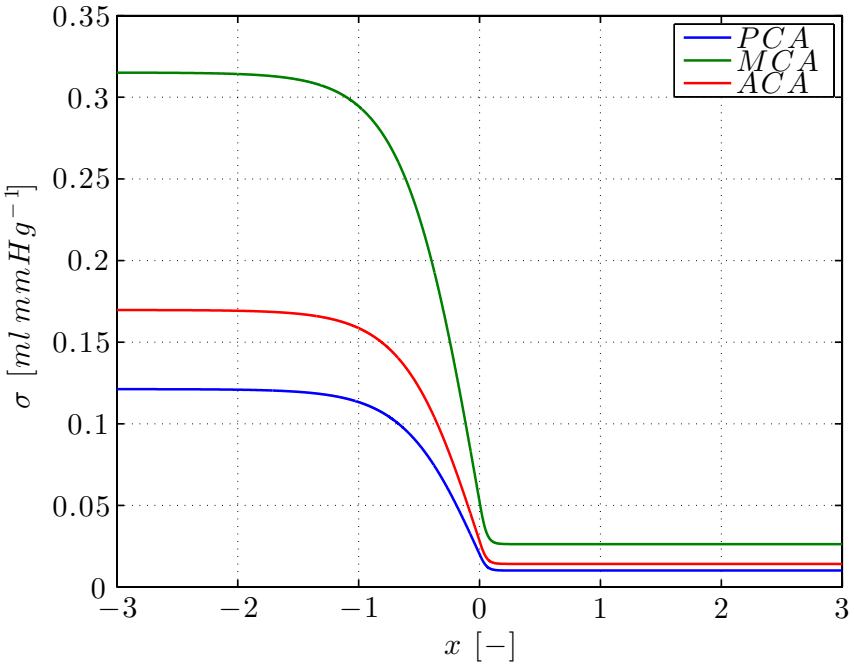

Figure 11: Sigmoidal curve σ_j over error signal x for large cerebral arteries

factor $4 \cdot C_{pa\,0,j}$.

Figure 11 shows the sigmoidal curve for all large cerebral arteries. For negative flow deviations, representing a decrease in tissue flow, the curve converges to the maximal vessel compliance. For a positive error signal, representing an increase in tissue flow, the curve converges to the minimal vessel compliance. The ability to dilate the vessel caliber is much larger than the ability to constrict. The saturation in vessel compliance represents the limit of the autoregulatory response. For $x_j \to -\infty \quad C_{pa\,max,j} = C_{pa\,0,j} + \Delta C_{pa\,max,j}/2$ and for $x_j \to \infty \quad C_{pa\,min,j} = C_{pa\,0,j} - \Delta C_{pa\,min,j}/2$. According to Eq. (16) and (19), the pial resistance is inversely proportional to the pial compliance. Any change in compliance leads to a change in resistance.

3.3 Implementation in MATLAB

In this section, the basic steps of solving the system equations are outlined. The final algorithm is implemented in MATLAB. This choice of programming environment facilitates a fast and simple implementation. The size of the 0D formulation allows to run the simulations on a personal computer.

The problem reduced to a set of nonlinear first order differential equations. The state variables of the model are the pial compliance C_{pa}, the intracranial pressure

P_{ic}, the venous pressure P_v, and the pial artery pressure P_{pa}. The input parameter of the model is either the inflow (cardiac output) or the pressure at the ascending aorta, depending on the test case. In the rest of this section, the cardiac output is considered the input parameter of the model.

The algorithm to solve the equations in time is comprised of the following steps.

1. At $t = 0$, the initial value of the state variables is set to: $C_{pa,j}(t) = C_{pa,j}(0)$; $P_{ic}(t) = P_{ic}(0)$; $P_v(t) = P_v(0)$; $P_{pa,j}(t) = P_{pa,j}(0)$
2. Read in input value for $q_{CO}(t)$ at current time step
3. Compute the pial volume and resistance $V_{pa,j}(t)$ and $R_{pa,j}(t)$ at the current time step
4. Calculate the 39 flows and 36 pressures in the model of the head and neck vessels at the current time step. The equations describing the Poiseuille flow in the head and neck vessels are written in matrix format $A(t) \cdot x(t) = b(t)$ and are solved for $x(t)$
5. Compute capillary pressure $P_c(t)$ and venous sinus resistance $R_{vs}(t)$
6. Calculate autoregulation parameters $q_{tiss,j}(t)$ and $\sigma_j(t)$
7. Compute state variables at next time step with time integration scheme: $C_{pa,j}(t + dt)$; $P_{ic}(t + dt)$; $P_v(t + dt)$; $P_{pa,j}(t + dt)$
8. Repeat steps 2)-7) as long $t < t_{end}$

In this work a forward Euler time discretization scheme is used combined with a time step of $\Delta t = 0.001\,\mathrm{s}$. This combination proofs to be stable for all simulations performed. For comparison, a backward Euler scheme in time with the Newton Raphson method was implemented. Both methods yielded the same results, the backward Euler method however required significantly more simulation time using the same time step size.

4 Results

4.1 Baseline values

In the first step, baseline values of the model presented in Section 3 are calculated. These baseline values represent average values for a healthy, young adult with a complete anatomy of the CoW at resting condition. The steady state solution of the model was calculated and the model parameters were adapted to fit the basal pressure and flow values reported in [14],[8]. All model parameters are summarized in Table 2. Under basal conditions, the hemodynamic quantities of the left and right side of the brain are considered symmetrical. The values for ACA, MCA, and PCA in Table 2 are therefore the same for left and right side. The venous sinus pressure P_{vs} is kept at the baseline value throughout all simulations.
Figure 12 shows the basal pressure and flow distribution in the proximal arteries and the circle of Willis. The mean cardiac output is set to $q_{co} = 88\,\mathrm{ml\ s^{-1}}$ at an aortic pressure of $P_a = 100\,\mathrm{mmHg}$. Approximately 80 % of the blood flow to the brain is supplied by the internal carotid arteries, 20 % by the basilar artery. The blood flow in the communicating arteries is two orders of magnitude smaller than in the large cerebral arteries. Under basal conditions, the perfusion of the brain is independent of the flow through the communicating arteries. The pressure at the end of all six large cerebral arteries ($P_{la\,0,j}$) is assumed to be equal.
The error signal that triggers the regulation mechanism is based on the deviation of the tissue flow $q_{tiss,j}$ compared to the basal values of the flow through the large arteries $q_{0,j}$, see Section 3.2. Under basal conditions the error signal is zero and the pial compliances and resistances remain constant.

4.2 Performance and limits of the cerebral autoregulation model

In this section, the impact of the autoregulatory response on pressure and flow distribution is investigated. In order to trigger the autoregulation mechanism, the pressure is increased uniformly throughout the cerebral vasculature by inducing a pressure step in the proximal aorta (P_a). A sudden increase in arterial pressure can be caused for example by a panic attack. Since the pressure step acts uniformly on the vasculature, changes in the right and left side of the brain are the same. The simulation has been carried out over 120 heart cycles. Assuming a normal heartbeat

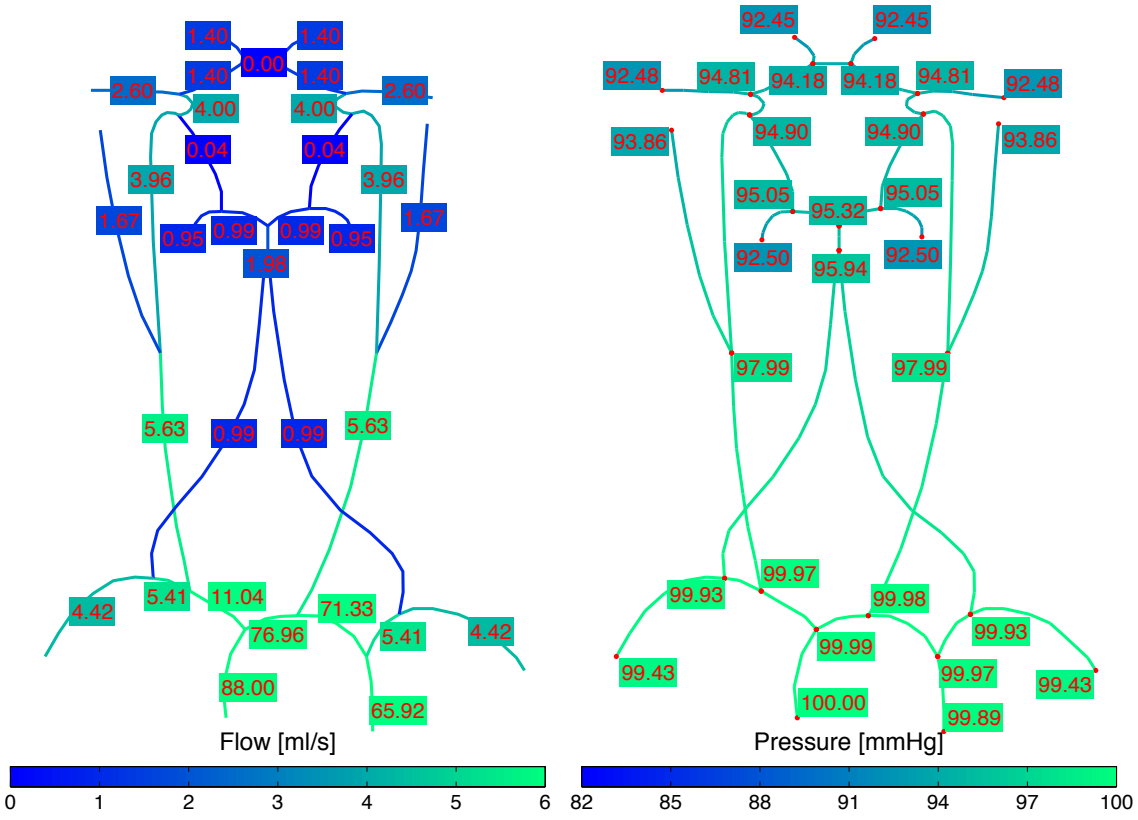

Figure 12: Baseline values for flow and pressure in the proximal arteries and the circle of Willis

Values of baseline pressures	
$P_{c\,0} = 25\,\text{mmHg}$	$P_{ic\,0} = 9.5\,\text{mmHg}$
$P_{la\,0,ACA} = P_{la\,0,MCA} = P_{la\,0,PCA} = 92.5\,\text{mmHg}$	$P_{v\,0} = 14\,\text{mmHg}$
$P_{pa\,0,ACA} = P_{pa\,0,MCA} = P_{pa\,0,PCA} = 58.75\,\text{mmHg}$	$P_{vs\,0} = 6\,\text{mmHg}$
Values of baseline flows	
$q_{0,ACA} = 1.40\,\text{ml s}^{-1}$	$q_{0,MCA} = 2.60\,\text{ml s}^{-1}$
$q_{0,PCA} = 0.95\,\text{ml s}^{-1}$	$q_{0,tot} = 9.90\,\text{ml s}^{-1}$
Values of baseline pial resistances and compliances	
$R_{pa\,0,ACA} = 49.0\,\text{mmHg s ml}^{-1}$	$R_{pa\,0,MCA} = 25.9\,\text{mmHg s ml}^{-1}$
$R_{pa\,0,PCA} = 70.9\,\text{mmHg s ml}^{-1}$	
$C_{pa\,0,ACA} = 0.028\,\text{ml mmHg}^{-1}$	$C_{pa\,0,MCA} = 0.053\,\text{ml mmHg}^{-1}$
$C_{pa\,0,PCA} = 0.020\,\text{ml mmHg}^{-1}$	
Constant model parameters	
$k_E = 0.11\,\text{ml}^{-1}$	$k_{ven} = 0.062\,\text{ml}^{-1}$
$\mu = 2.775e-05\,\text{mmHg s}$	$P_{v1} = -2.5\,\text{mmHg}$
$R_{pv} = 1.116\,\text{mmHg s ml}^{-1}$	$R'_{vs} = 0.456\,\text{mmHg s ml}^{-1}$
$R_f = 2325.23\,\text{mmHg s ml}^{-1}$	$R_o = 525.05\,\text{mmHg s ml}^{-1}$
Regulation parameters	
$G = 2.0$	$\tau = 20\,\text{s}$
$\Delta C_{pa\,min,j} = C_{pa\,0,j} \qquad j = 1,..,6$	$\Delta C_{pa\,max,j} = 10 \cdot C_{pa\,0,j}$

Table 2: Baseline values of hemodynamic quantities and model parameters for the 0D-model of the cerebral vasculature

of 75 Hb/min, the interval of one heart cycle results to $t = 0.8\,\mathrm{s}$, amounting to a total simulation time of $T = 96\,\mathrm{s}$. Throughout all simulations, the model is operated on cycle-mean pressure and flow values only. The initial value of all state variables is set to the baseline values presented in Table 2. The boundary condition at the end of the right and left brachial and thoracic aorta, as well as both external carotid arteries, is set to a prescribed flow ratio in accordance with the baseline flow distribution in Section 3.1.2.
Figure 13a shows the prescribed input pressure step of $\Delta P_a = 20\,\mathrm{mmHg}$ over time. This pressure step leads to an instantaneous increase in flow in the large cerebral arteries, see Figure 13b. The deviation of the flow from the baseline value subsequently triggers the autoregulation mechanism, which helps to recoup most of the initial flow. According to Eq. (23),(24),(25), an increase in flow leads to a direct decrease in pial compliance, see Figure 13c. In this simulation, all six cerebral arteries encounter the same percentage of change relative to the initial value. Since the middle cerebral artery is the largest cerebral artery, it carries the largest part of the total pial compliance and therefore has the largest quantitative change in compliance. Based on Eq. (19), a decrease in pial compliance leads to an increase in pial resistance, Figure 13d. According to Poiseuille's Law, an increase in resistance leads to a decrease in flow after the pressure step. Again, the relative change in resistance with respect to the initial value is the same in all cerebral arteries. Since the posterior cerebral arteries are the smallest, the pial resistance there is the largest. Figure 13e shows the intracranial and venous pressure P_{ic} and P_v over time. The venous pressure depends on the change in intracranial pressure and exhibits therefore the same characteristics, Eq. (11). The ability to restore the pressure after the step increases with distance to the pial arteries in the flow direction. Figure 13f illustrates the pial pressure P_{pa} over time. Only a small percentage of the pressure step can be restored. In this scenario, the pial pressure is uniform in all cerebral arteries.

The response of the autoregulation takes place in the time frame of seconds. The compliances, resistances, and flows converge directly after the imposed change in pressure to a constant value. Figure 14 shows again the development of the intracranial pressure over time after a prescribed increase in arterial pressure. Here, the simulation was run for 1250 cycles, which equals a total simulation time of $T = 1000\,s$. After the initial increase in P_{ic}, caused by the increase in P_a, the autoregulation response decreases the intracranial pressure below the normal baseline value. Subsequently, the intracranial pressure slowly increases, converging towards

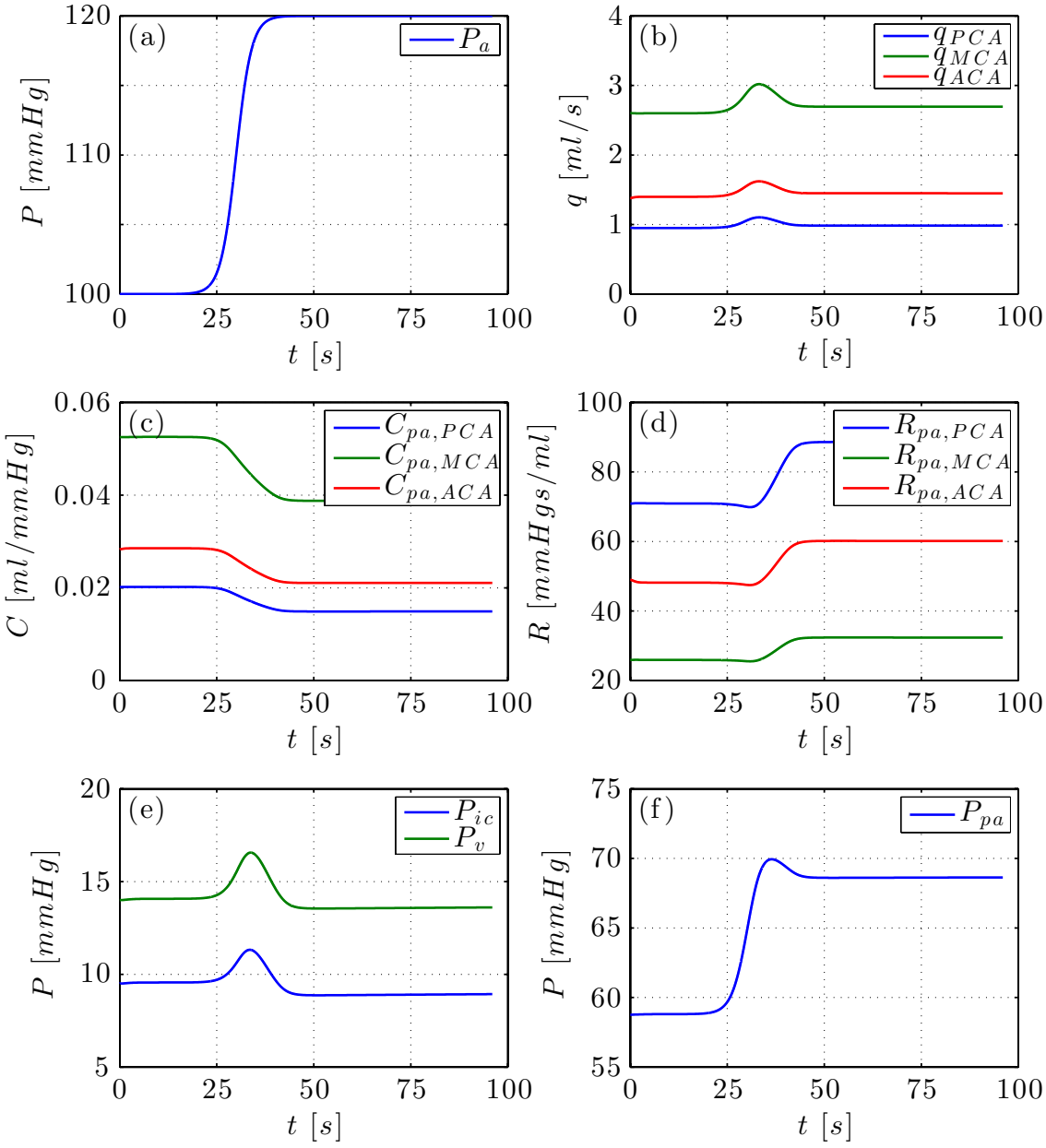

Figure 13: Response of state variables and the autoregulation mechanism to a sudden increase in arterial pressure P_a

the baseline value. In comparison to the autoregulation response, the convergence of the intracranial pressure takes up to several minutes. The intracranial pressure is defined by the volume equilibrium of the cranial space, comprised of the brain tissue, the cerebral blood volume, and the cerebrospinal fluid (see The Monro-Kellie hypothesis, Section 2.1). The autoregulation causes the pial compliances to decrease in order to restore the baseline flow. This drop in compliance leads to a decrease in cerebral blood volume, which causes a drop in intracranial pressure below the normal baseline value. In order to restore the cranial volume equilibrium, the cerebrospinal fluid volume has to increase, compensating the loss in blood volume. The change in cerebrospinal fluid is controlled by the cerebrospinal fluid production and reabsorption. Figure 15 shows the values of $q_{CSF,production}$ and $q_{CSF,reabsorption}$ over the simulation time. The CSF production is constant shortly after the autoregulation response at a level above the initial value. The CSF reabsorption on the other hand decreases after the pressure drop below the CSF production level. This difference leads to an increase in CSF volume, restoring the equilibrium and increasing the intracranial pressure back to its initial baseline level. This process takes several minutes, since $q_{CSF,production}$ and $q_{CSF,reabsorption}$ are 3 orders of magnitude smaller than the cerebral blood flow. The cranial space is again at volume equilibrium when the CSF reabsorption converges towards the CSF production level.

In the following simulations, the pressure step ΔP_a is further altered in order to investigate the limits of cerebral autoregulation. In Figure 16, the normalized flow in the middle cerebral artery over the mean arterial pressure is presented. For each value of arterial pressure change, the autoregulatory response is simulated and the converged normalized flow value is plotted (blue dots). Between arterial pressures of 70 and 150 mmHg the autoregulation mechanism is able to maintain a nearly constant blood flow. For arterial pressures beyond these limits, the vasculature is not able to adapt its compliance and resistance any further, resulting in a large change in flow. These simulation results are compared to experimental data from *Harper et al.* [9] and *Dirnagl et al.* [7]. Both datasets are acquired from experiments performed on rats, measuring the cerebral microvascular pressures and blood flow as the systemic arterial pressure is altered. The simulation results are consistent with the experimental results, capturing the important characteristics of the autoregulatory response. The resulting autoregulation curve is the same for all cerebral arteries, since during a uniform pressure change the relative change in vessel caliber is assumed equal in all arteries.

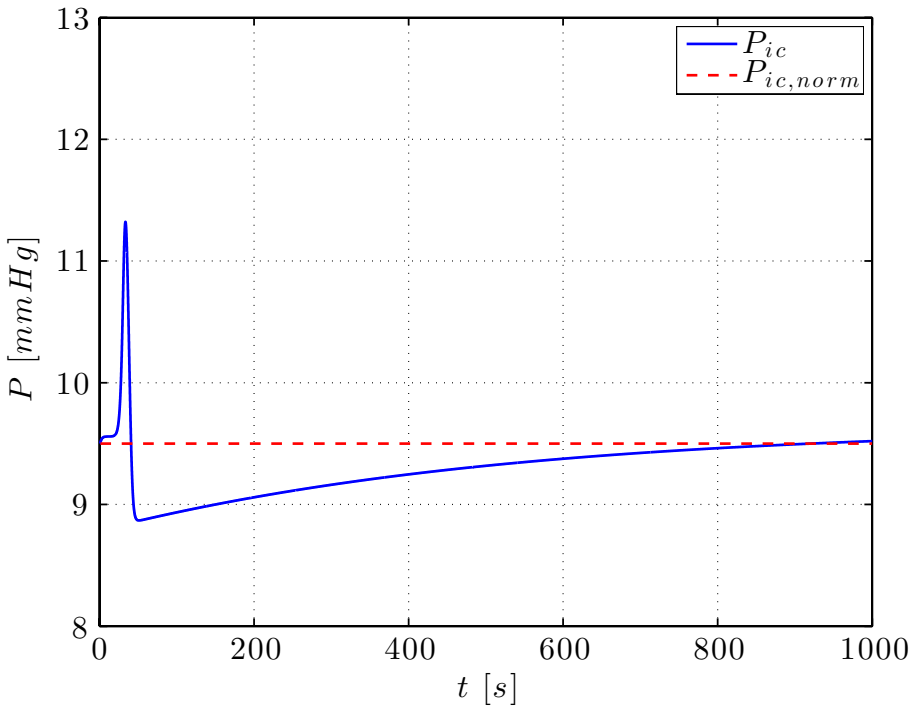

Figure 14: Recovery of the intracranial pressure after a sudden increase in aterial pressure

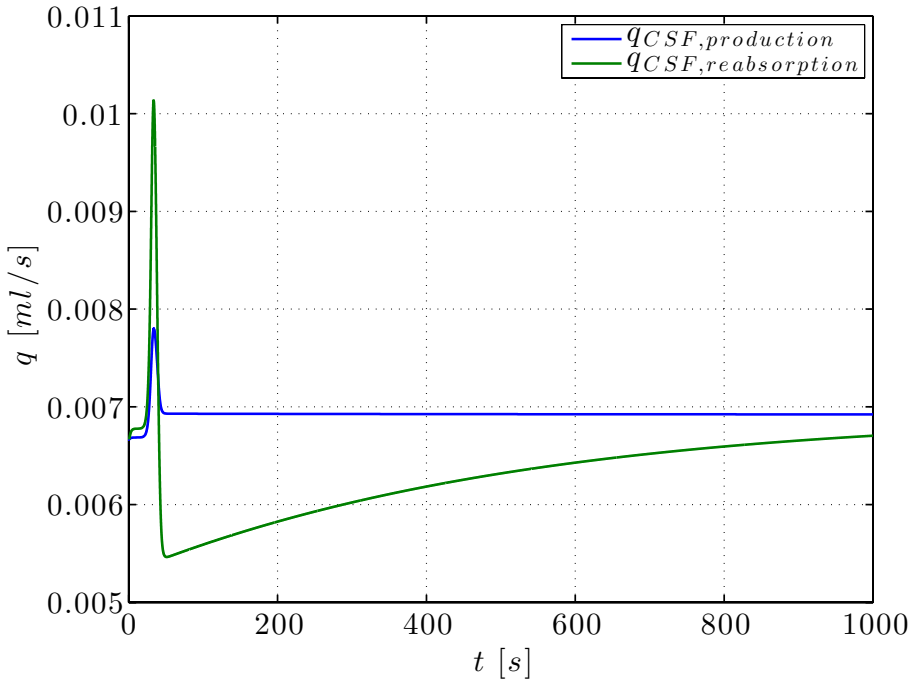

Figure 15: Cerebrospinal fluid production and reabsorption after increase in arterial pressure

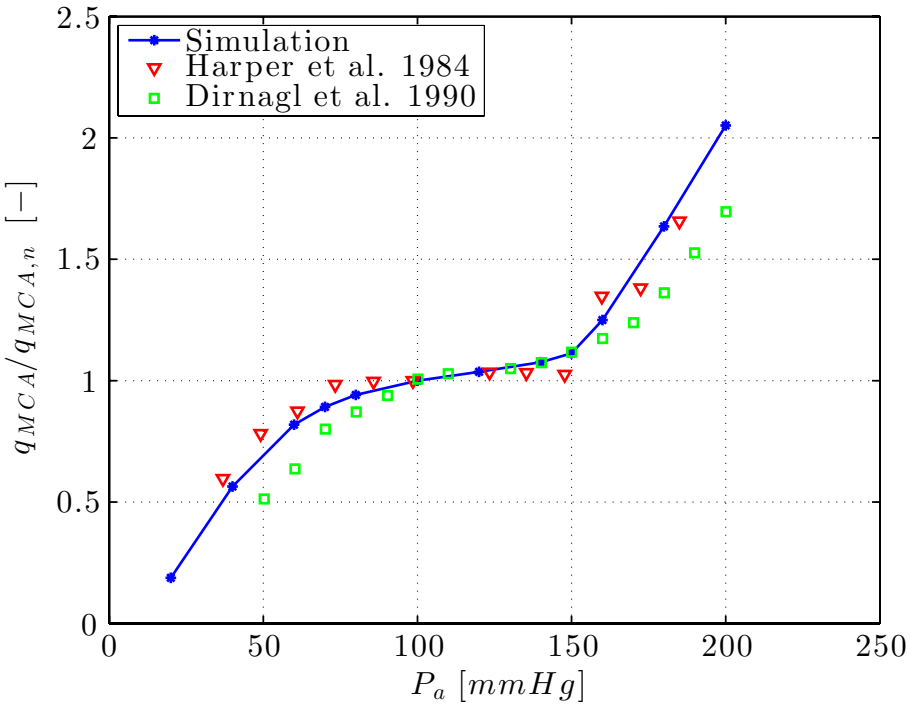

Figure 16: Autoregulatory response over a range of arterial pressures

4.3 Simulation of cerebral flow autoregulation following carotid clamping during endarterectomy

In this section, the lumped parameter model of the cerebral vasculature is used to simulate the autoregulation in cerebral flow following the clamping of the right carotid artery during an endarterectomy. In Section 2.3, the basic steps of this procedure were outlined. In the following subsections, common scenarios with varying severity of blocked vessels and missing cerebral arteries are presented. The goal of these simulations is to investigate the brain's capability to compensate a sudden loss in blood flow to the brain.

Throughout all simulations, the cardiac output is kept constant at $q_{co} = 88\,\mathrm{ml/s}$. This assumption is justified because the heart is kept fully functional during anesthesia in order to provide sufficient flow to the brain. The simulation is carried out over a total simulation time of $T = 85\,\mathrm{s}$ with a time step of $\Delta t = 0.001$.

The vasculature distal of the aorta and the brachial arteries has the ability to adapt to changes in in blood volume through its compliance. The pressures at the end of the right end left brachial artery and thoracic aorta are therefor approximately

constant. For this reason, these pressures are set to the normal baseline values throughout the simulations. A flow ratio is prescribed for the boundary condition at the external carotid arteries. The mean velocity ratio between the ICA and CCA under normal conditions is $\frac{V_{ICA}}{V_{CCA}} = 1.05$, see Section 3.1.2. These choices of boundary condition are further discussed in Section 5.1.

4.3.1 Stenosed right carotid artery

In this first example, a patient with a stenosed right carotid artery is considered. As shown in Section 2.3, the stenosis is typically located at the bifurcation of the CCA. The biggest part of the stenosis is assumed to be in the ICA with a length of 4cm. The CCA and the ECA are also affected by the stenosis with a length of 2cm each. The stenosed parts of the carotid artery are assumed to have a mean 85 % reduction on cross section. The resulting resistance in the three carotid arteries is calculated according to Eq. (22). The patient is assumed to have a complete anatomy of the circle of Willis. These narrowed arteries lead to new baseline values for flow and pressure, presented in Figure 17. Compared to the normal baseline values shown in Figure 12, the flow through the narrowed right CCA is severely decreased. This loss in blood flow is compensated through two channels. First, the collateral pathways of the circle of Willis are used to redirect flow to the regions normally perfused by the right ICA. The remaining three healthy arteries supplying the CoW (left CCA, right and left VA) are increasingly perfused in order to compensate the loss in blood flow in the right CCA. The flow is then redirected through the anterior and posterior communicating arteries to supply the right anterior and middle cerebral artery. While being idle for a healthy subject, the communicating arteries play a pivotal role in the case of a diseased patient. The flow is redirected through a path with a higher resistance than the path under normal baseline conditions, which results in a higher pressure loss. The second channel to ensure sufficient blood flow to the brain is the autoregulatory mechanism at the level of the pial arteries. The narrowing of the right CCA leads to an increase in compliance and a decrease in resistance to increase flow through the large cerebral arteries. The system is already borrowing some of the vascular capacity to ensure baseline flow. This means that the vasculature has less regulatory reserve to compensate flow loss during a clinical procedure.

In the next step, we simulate that this patient undergoes a carotid endarterectomy in order to remove the plaque that causes the narrowing. The simulation entails the clamping of the right carotid artery during the surgical procedure and the following

adaptation of the vasculature to this sudden loss in blood flow. The initial values for the simulation are set to the new baseline values. Figure 18 shows the converged values for flow and pressure in the circle of Willis after the clamping. The flow through the right carotid artery has stopped completely and is redirected through the rest of the vasculature. The transient evolution of the state variables during the clamping procedure is shown in Figure 19. The clamping of the right carotid artery is simulated by decreasing the radius of the right CCA via a smoothed step function. Figure 19a shows the radius of the right CCA over time. Figure 19c,d indicate that the largest change in pial compliance and resistance happens in the right middle and anterior cerebral arteries, which are the most affected by the clamped carotid artery. In the normal baseline pressure distribution of a healthy subject, the pial pressure is the same in all large cerebral arteries. Figure 19f illustrates the varying changes pial pressures in the large cerebral arteries.

In the case of the presented patient with a narrowed right carotid artery, the cerebral vascular system is able to compensate the loss in blood flow to the brain during the clinical procedure of a carotid endarterectomy. The deviation of blood flow in the large cerebral arteries after the clamping compared to normal baseline values is around $1 - 2\,\%$, see Table 3.

4.3.2 Stenosed carotid and vertebral arteries

For this next example, a patient with stenosed right and left carotid arteries and right and left vertebral arteries is chosen. The stenosis in both carotid arteries is modeled with a $85\,\%$ narrowed cross section, exactly as in the previous example. In both vertebral arteries a $4\,\text{cm}$ long stenosis with a $75\,\%$ narrowed cross section is assumed. This is a more extreme but not uncommon scenario. The circumstances that led to a stenosis in the first place commonly lead to plaque deposits in multiple location in the vasculature. The anatomy of the circle of Willis is again complete. The patient's disease pattern leads to new baseline hemodynamic values, presented in Figure 20. The blood flow in the four supplier vessels is forced through an increased resistance caused by the narrowing, resulting in a decreased flow to the brain and an increased flow to the lower body. This results in a large pressure drop in the circle of Willis and the distal arteries. The pial compliances and resistances also change greatly to compensate for the blood loss. The decrease in CBF of the new compared to the normal baseline condition is around $10\,\%$.

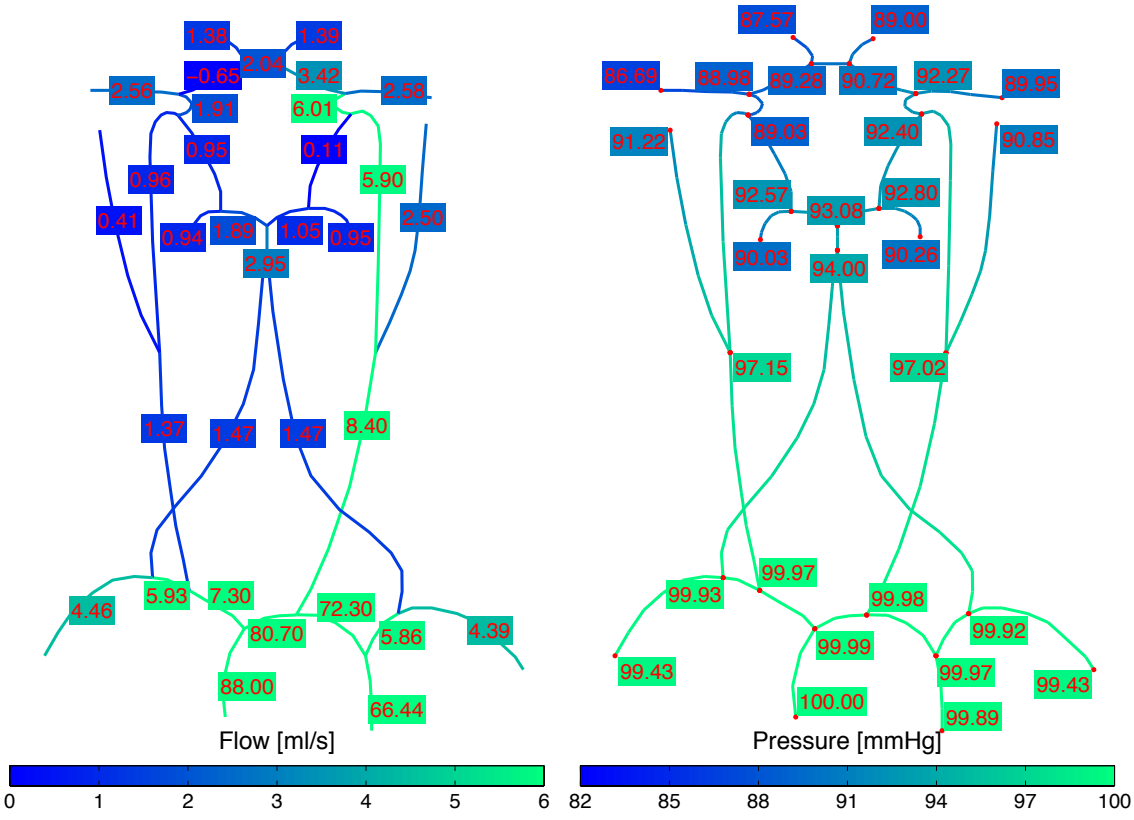

Figure 17: New baseline flow and pressure distribution in the CoW for a patient with a 85 % stenosed right carotid artery

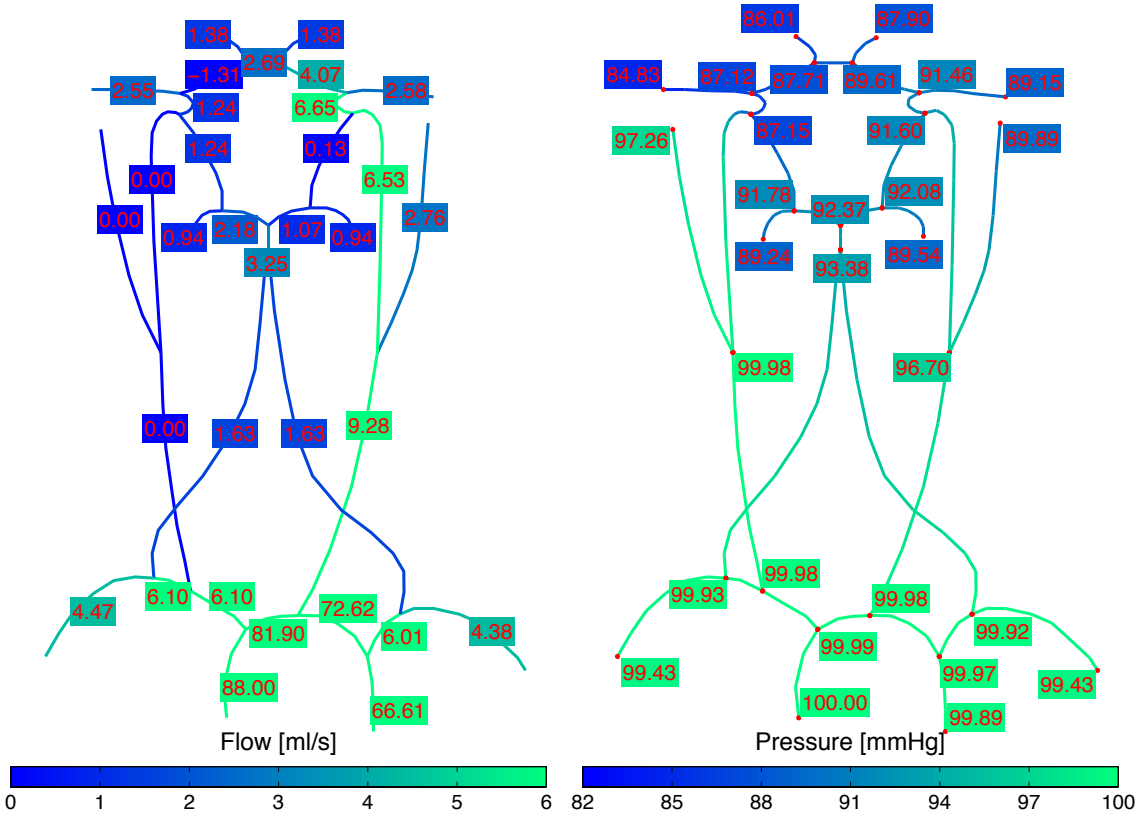

Figure 18: Flow and pressure distribution in the CoW for a patient with a 85 % stenosed right carotid artery after the clamping of the right carotid artery

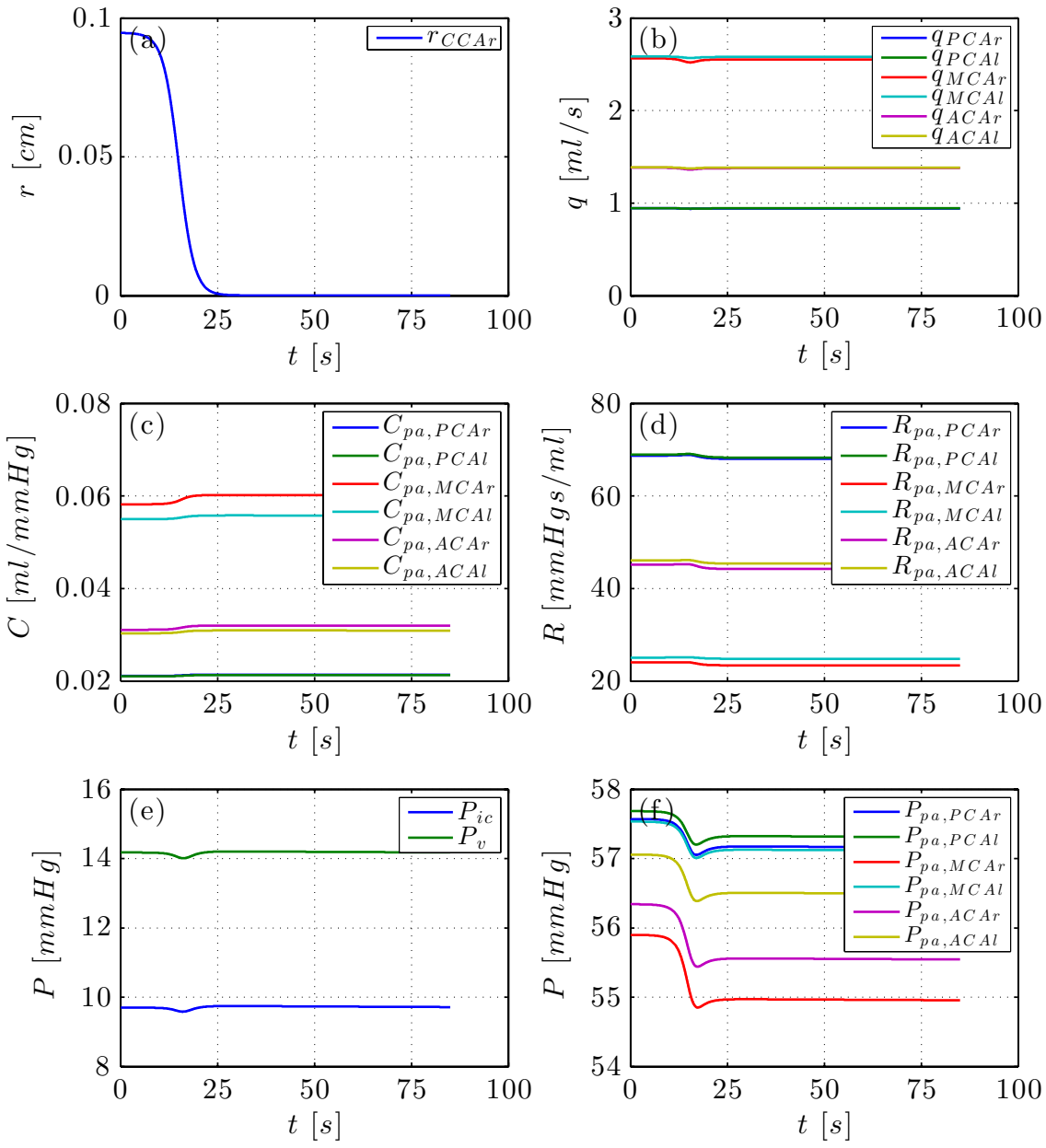

Figure 19: Response of the state variables during the clamping of the right carotid artery for a patient with a stenosed right carotid artery

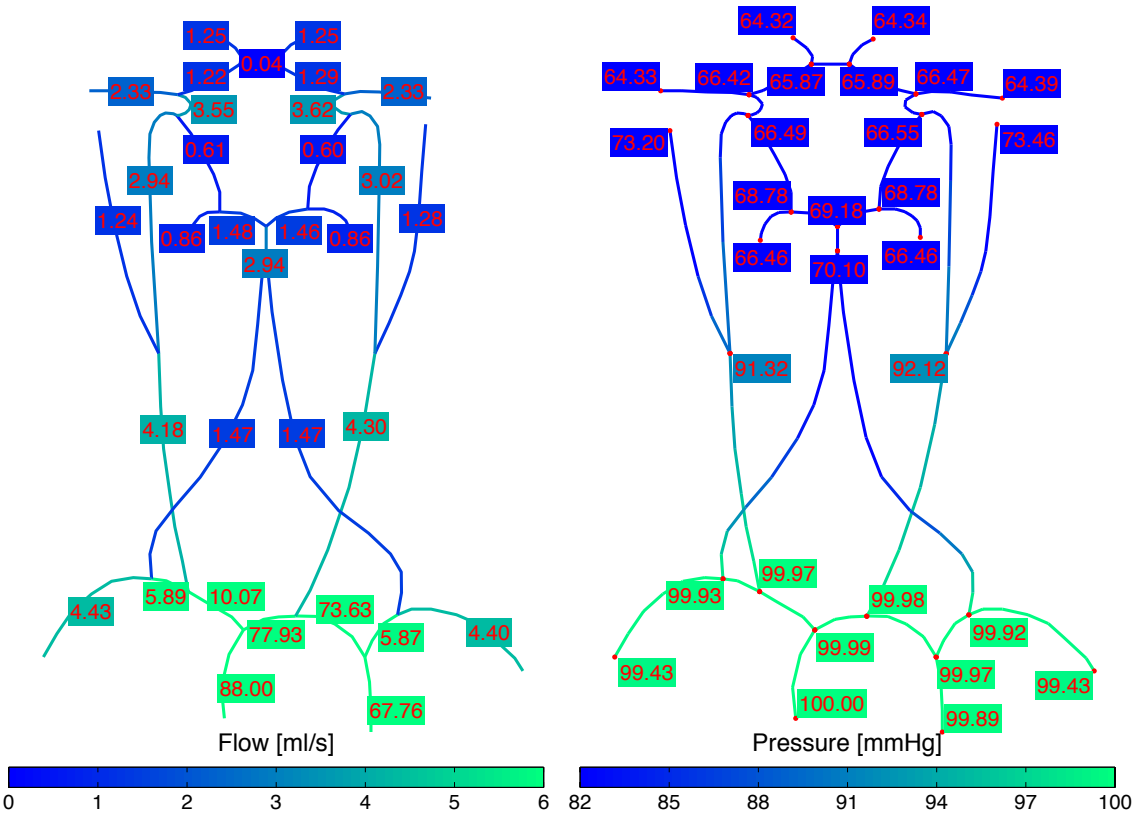

Figure 20: New baseline flow and pressure distribution in the CoW for a patient with 85 % stenosed CAs and 75 % stenosed VAs

The simulation of the clamping of the right carotid artery leads to the flow and pressure distribution shown in Figure 21. The loss in flow in the large cerebral arteries compared to the normal baseline values is approximately 20 % (Table 3). Figure 22 shows the transient behavior of the state variables. The drop in flow and pressure after the clamping is larger than in the previous example. Figure 22b shows the flow in the large cerebral arteries over time. Only a small part of the flow drop after the clamping can be recovered. The system is close to the autoregulatory limit.

4.3.3 Stenosed carotid and vertebral arteries in combination with a missing right PCoA and contralateral PCA,P1

In this last example, a patient with stenosed carotid and vertebral arteries, exactly as presented in the previous example, is investigated. In the last two examples, the subject was assumed to have a complete anatomy of the circle of Willis. In reality, only about 50 % of people have a complete anatomy of the circle of Willis [13]. Here in this example, an anatomy is considered with a missing right posterior communicating artery (PCoA) and P1 segment of the left posterior cerebral artery

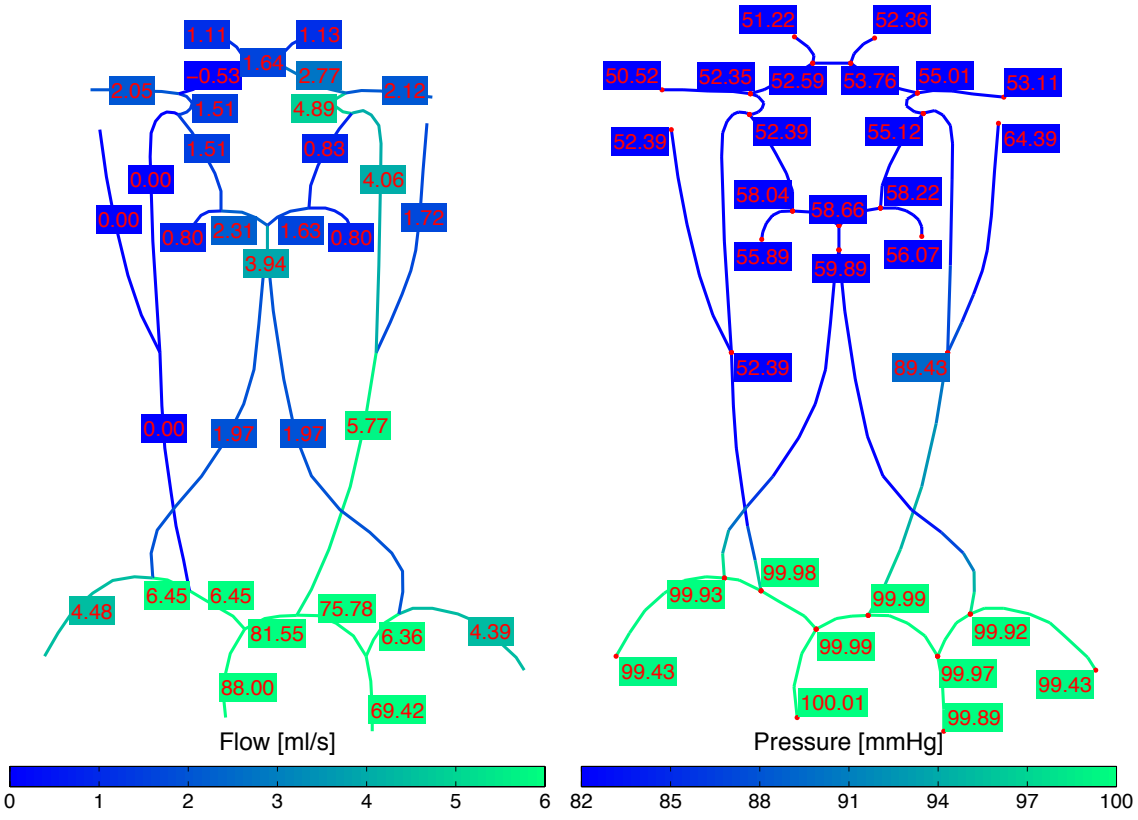

Figure 21: Flow and pressure distribution in the CoW for a patient with 85 % stenosed CAs and 75 % stenosed VAs after the clamping of the right carotid artery

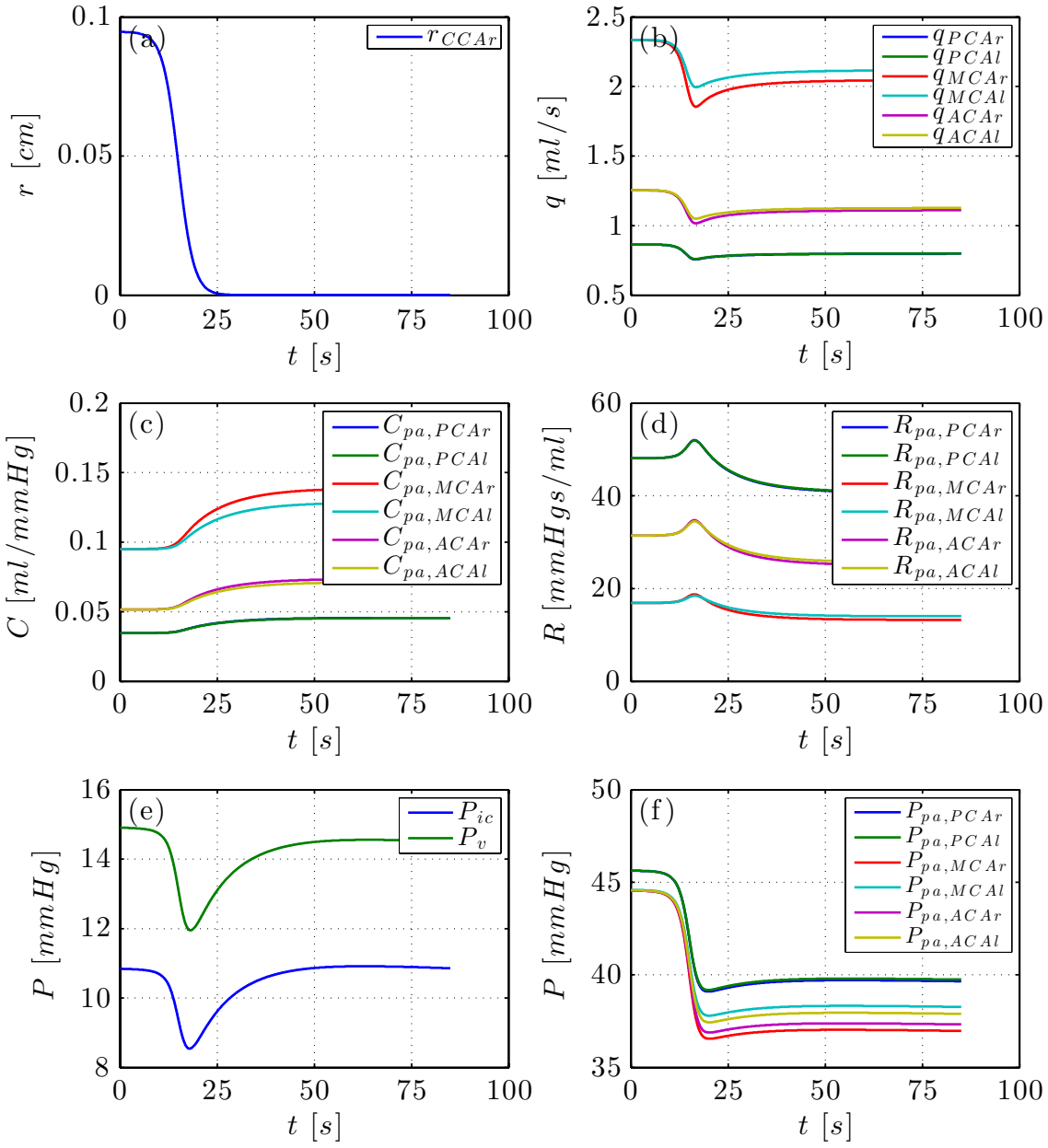

Figure 22: Response of the state variables during the clamping of the right carotid artery for a patient with stenosed CAs and VAs

(PCA,P1). According to [13], approximately 9% of people have this anomaly. The new baseline values for flow and pressure in the circle of Willis are shown in Figure 23. In this configuration, the right posterior cerebral artery is completely isolated from the circle of Willis and is therefore perfused by the two vertebral arteries. The rest of the cerebral vasculature is perfused only by the two internal carotid arteries. Since both ICAs are severely narrowed the blood flow to the rest of the cerebral arteries decreases significantly compared to the normal baseline condition (15 %).

Again, the procedure of carotid clamping during an endarterectomy is simulated. In Figure 24 the flow and pressure results are shown. The right PCA is still perfused well by the VAs. After the clamping of the right carotid artery, the entire flow for the remaining 5 cerebral arteries is supplied by the left carotid artery. This results in a great decrease in flow in middle cerebral (right: 44.2 %, left: 36.2 %), anterior cerebral (right: 42.1 %, left: 38.6 %), and left posterior cerebral artery (41.1 %). In Figure 25, the response of the state variables is shown. Except for the right PCA, the pial compliances and resistances of the remaining CAs are close to their capacity limits. The vaculature is unable to recover most of the loss in CBF. The pial pressure P_{pa} drops greatly in all CAs except of the right PCA, Figure 25f.

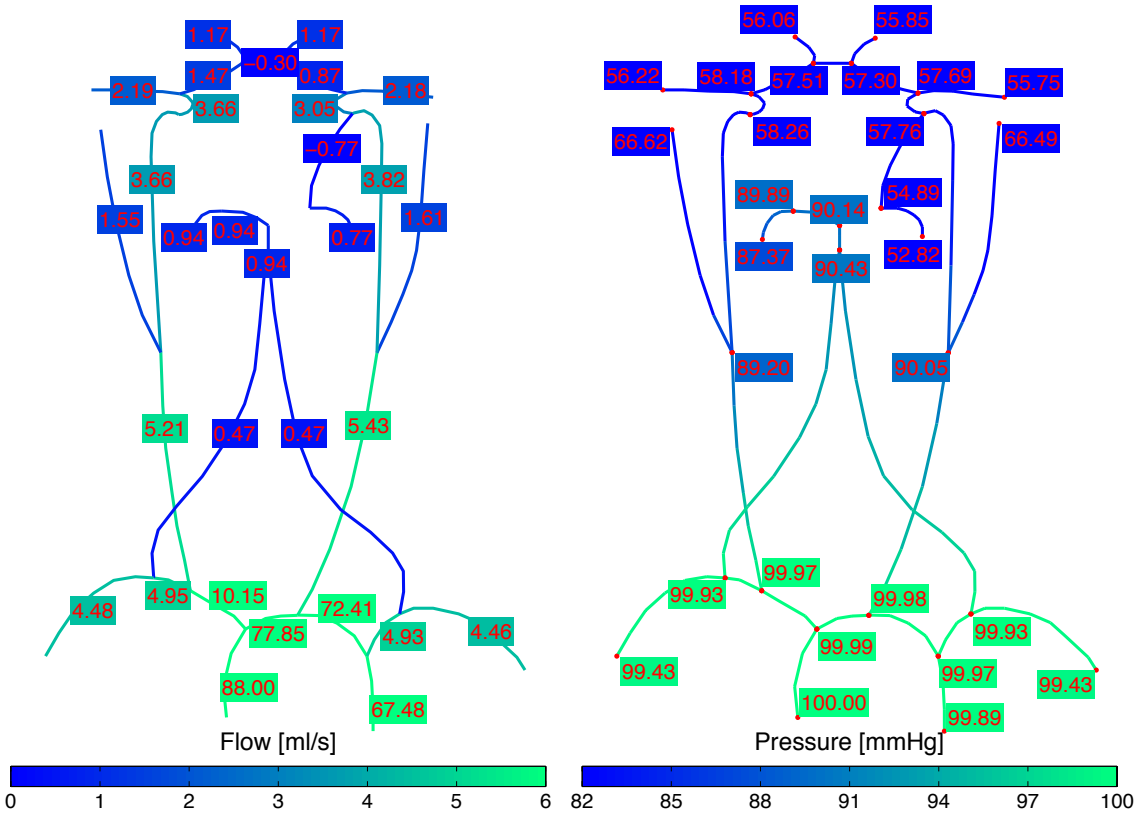

Figure 23: New baseline flow and pressure distribution for a patient with stenosed CAs and VAs combined with missing PCoA and PCA,P1

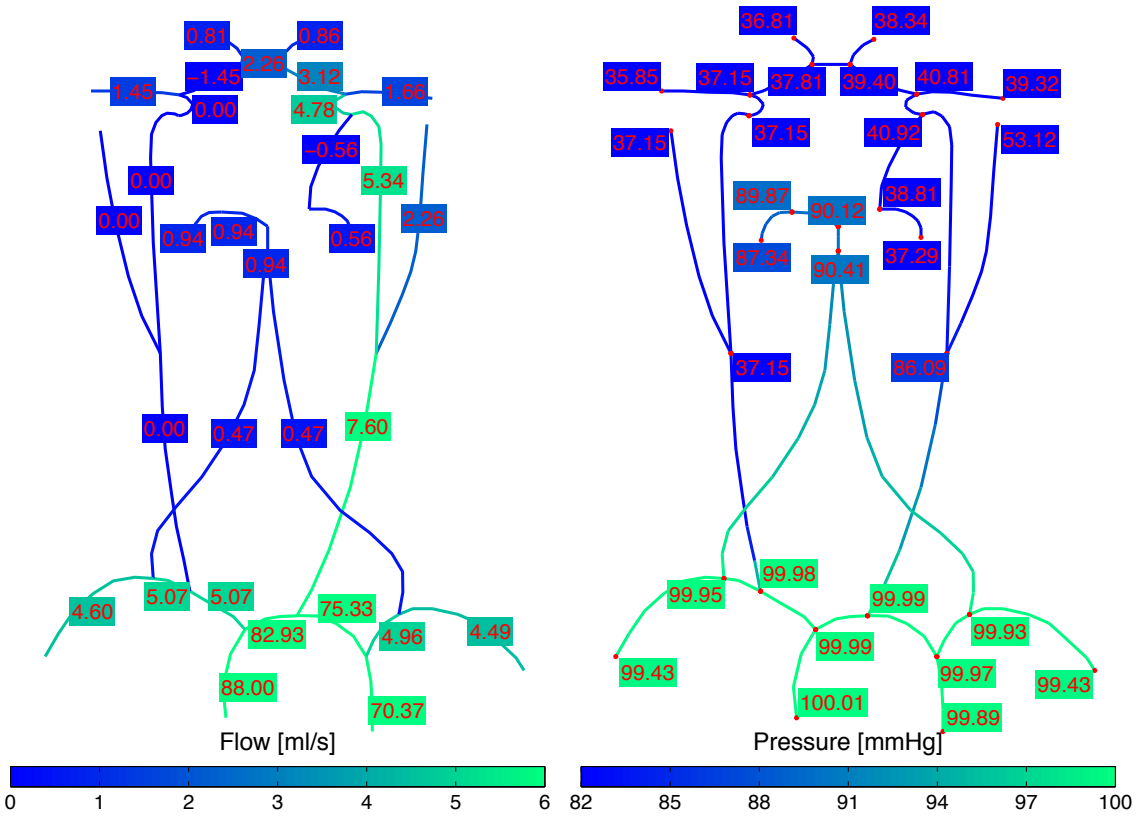

Figure 24: Flow and pressure distribution after the clamping of the right carotid artery. Patient has stenosed CAs and VAs in combination with missing PCoA and PCA,P1

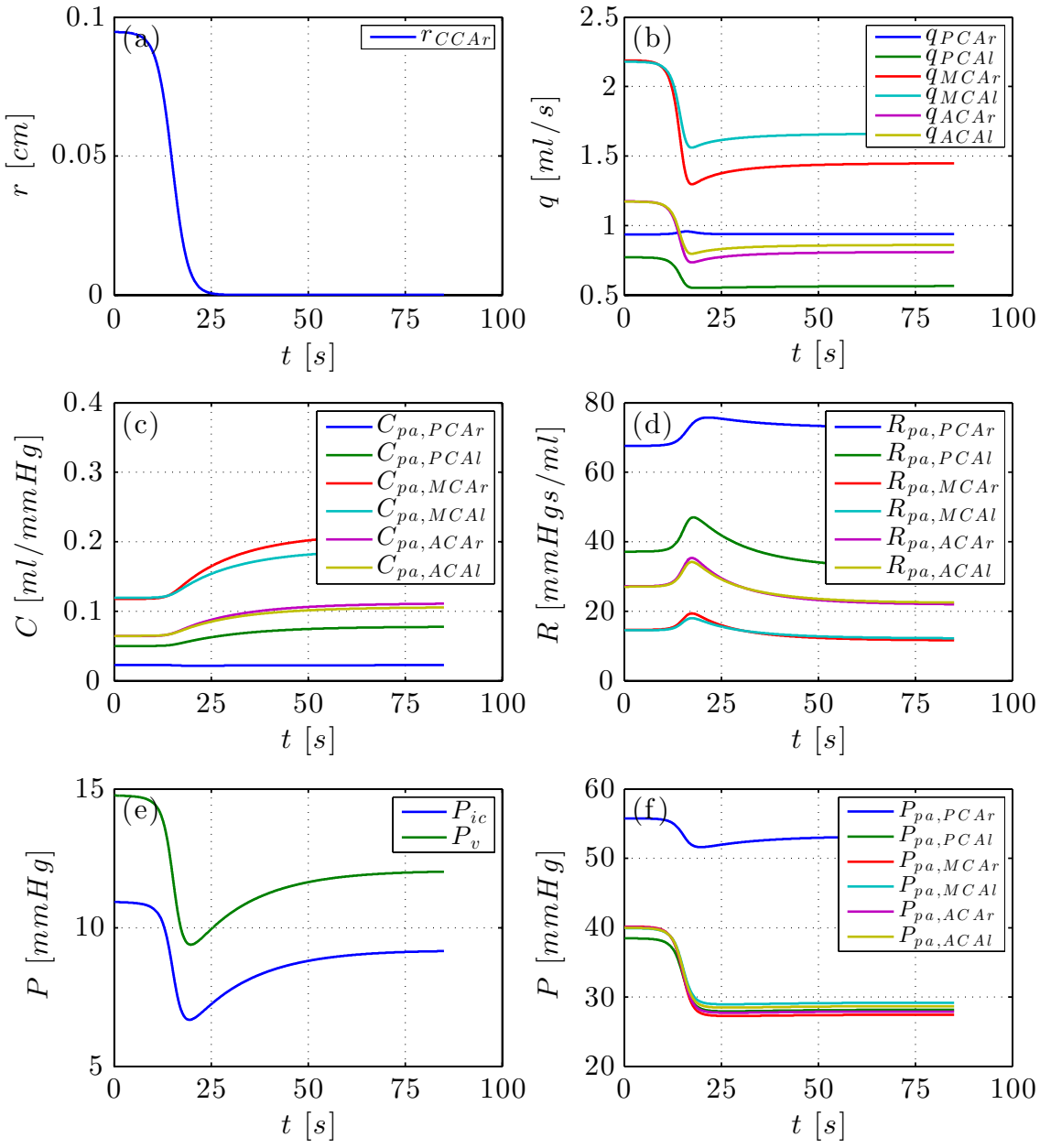

Figure 25: Response of the state variables during carotid clamping for a patient with stenosed CAs and VAs in combination with missing PCoA and PCA,P1

	ACAr	ACAl	MCAr	MCAl	PCAr	PCAl
85% rCA - baseline	-1.4%	-0.7%	-1.5%	-0.8%	-1.1%	-0.0%
85% rCA - clamped	-1.4%	-1.4%	-1.9%	-0.8%	-1.1%	-1.1%
85% CAs + 75% VAs baseline	-10.7%	-10.7%	-10.4%	-10.4%	-9.5%	-9.5%
85% CAs + 75% VAs clamped	-20.7%	-19.3%	-21.2%	-18.5%	-15.8%	-15.8%
85% CAs + 75% VAs PCoA; PCA,P1 - baseline	-16.4%	-16.4%	-15.8%	-16.2%	-1.1%	-18.9%
85% CAs + 75% VAs PCoA; PCA,P1 - clamped	-42.1%	-38.6%	-44.2%	-36.2%	-1.1%	-41.1%

Table 3: Drop in blood flow relative to the normal baseline values for all six large cerebral arteries. Both changes of the new baseline values and changes after carotid clamping are shown

5 Discussion

5.1 0D-model of the cerebrovascular system

In Section 4.1, the baseline values for flow in the circle of Willis are based on average values found in the literature. These values have been measured in vivo, for example via Doppler velocity measurements. Comparing the measured values for the inflow through the ICAs and the VAs to the measured values for the outflow through the ACAs, MCAs, and PCAs results in $q_{in} \neq q_{out}$. Only about 2/3 of the inflow leaves the brain through the six large cerebral arteries. For simplicity, only the large cerebral arteries are considered in our model, neglecting the outflow though the small cerebral arteries. Two examples of the neglected arteries are the superior cerebellar artery and the anterior inferior cerebellar artery. In order to satisfy the mass conservation of the model equations, the baseline values present a compromise between averaged measured values for in- and outflow. All baseline values for flow presented in Section 4.1 are in the range of measured values reported in [8].

The right choice of boundary conditions for the right and left brachial arteries as well as for the distal aorta is very important in order to reproduce physiological scenarios. In Section 4.2, the ratio between cardiac output and the flow to these three arteries is kept constant at the baseline value from Section 4.1. In the simulations, the aortic input pressure is varied, leading to a change in cardiac output. It is assumed that for a drop in cardiac output the flow decreases uniformly in all large arteries of the vasculature. This assumption can be reproduced with this choice of boundary conditions.
For the simulations in Section 4.3, the boundary conditions are changed. Throughout the simulations the cardiac output is kept constant. The stenosis and the clamping of the right carotid artery lead to a decrease in blood flow to the brain. This decline in blood flow is compensated by an increase in perfusion to the arms and the distal aorta. In this case the pressure at the end of the right and left brachial arteries and of the distal aorta is kept constant at baseline value. This assumption is based on the idea that the storage capacity of the vasculature distal of the aortic arch compensates the increase in blood flow by expanding the vessel caliber. In the case of ideal compensation of the increased flow the pressures in the proximal aorta stay constant at baseline value. This approach is a strong simplification of reality. An improved boundary condition would be the use of a 3-element Windkessel model instead of the constant pressure BC. The 3-element WK accounts for the change in

blood volume though the compliance.

The autoregulation model is tested extensively in Section 4.2. In Figure 13 the autoregulatory response of the cerebral vasculature to a sudden increase in pressure is shown. The decrease in pial compliance and the concomitant increase in pial resistance, as described by Eq. (23), helps to restore most of the baseline flow. Shown in Figure 16, the cerebral autoregulation allows to maintain approximately constant perfusion to the brain in the limits of normal arterial pressure values. The autoregulation model captures the important characteristics of the autoregulation response, which are well within reported experimental values. This model is designed to account for the autoregulatory feedback response caused by changes in CBF only. The phenomenological-based response does not distinguish between the different regulatory mechanisms contributing to the nonlinear response of the VSM. In this project, we are only interested in the ultimate response of the cerebral vasculature, and not in the underlying physiological mechanisms which generated this response. However, there are several features of cerebral autoregulation that are not included in the current model, but which are very important. In reality, the metabolic response reacts to changes in oxygen levels in the blood and to changes in oxygen demand. For example, the brain's need for oxygen is significantly lower under general anesthesia than under normal conditions. This means that the needed blood supply to the brain during the time of the anesthesia is reduced. Closely coupled to the metabolic response is the neurogenic response. Changes in brain activity have a direct influence on the oxygen demand. In contrast to the metabolic response, the neurogenic response is a feedforward mechanism. At the onset of a change in brain activity, this mechanism sends a fast signal to the VSM in the pial arteries. This allows a change in pial resistance and compliance before a sudden change in flow occurs and thereby decreases the temporal change in flow.

The simulations performed in this work are all based on cycle-average flow and pressure input values. The goal of this thesis is to investigate the response of the state variables over the course of approximately one minute after the activation of the autoregulatory mechanism. Here, the primary interest is in the main trend of the response. However, pulsatile pressure and flow values provide additional information about the effect of the changing compliance on the pulse pressure. Blood volume is stored in the vessels during systole and subsequently released during diastole, thereby damping the pulsatile flow. The part of the model which represents the

small arteries, veins, and intracranial space accounts for changes in cerebral blood volume through several capacitors. The 0D-representation of the circle of Willis and the proximal arteries on the other hand only accounts for viscous losses through resistances. For simplicity, the change in cerebral blood volume is neglected in this part of the model. Due to the large amount of elastin, the large arteries exhibit large changes in compliance during systole. The simulation of pulsatile flow and pressure values requires the consideration of the large vessel's compliance properties in the model. The evaluation of the error signal for the autoregulation model continues to work on cycle-averages values.

5.2 Simulation of carotid endarterectomy

The stenosis and the clamping of the carotid artery lead to significant changes in perfusion to the external carotid arteries. In Figure 18 the converged flow distribution in the CoW after the clamping is shown for the case of a 85 % stenosed right carotid artery. Due to the completely blocked right carotid artery, the bulk of flow is redirected through the left carotid artery. This results in a 65 % flow increase in the left ECA and a complete loss in flow in the right ECA. The external carotid arteries supply the neck and the face with blood. While our brain must be perfused properly during all times, the level of blood flow to the face is not as critical. The tissue in the facial and neck regions can endure severe changes in perfusion for a short amount of time without permanent damage. In reality, the small arteries, supplied by the ECA, also have some autoregulatory mechanism to adapt the vessel diameter in the case of a change in perfusion. However, these autoregulatory capacities are not as pronounced as in the large cerebral arteries and therefore neglected in this model. In addition there is collateral flow at the level of the small arteries. In the case of a completely blocked ECA, there is still flow going to the small arteries and the tissue normally perfused by the ECA. This collateral flow is however only a fraction of the flow going through the ECA under baseline conditions. Again, this collateral network is therefore not incorporated into this model.

In Section 4.3, three patient examples with varying severity of stenosis are presented. In the case of single stenosed carotid artery in combination with a complete anatomy of the circle of Willis, the vasculature is able to compensate the loss in blood flow during the clamping of an endarterectomy. In this case, the use of a shunt is not necessary to ensure sufficient perfusion to the brain during the surgical procedure. In the case of the patient with stenosis in both carotid and vertebral arteries the

cerebral vasculature is able to maintain 90 % of the normal baseline flow to the six large cerebral arteries under baseline conditions. Considering the severity of the disease this is quiet remarkable. During the procedure, the clamping of the right carotid artery leads to an additional loss in blood flow, resulting in a flow deviation of around 20 % in the large cerebral arteries. In the last patient example, a severe stenosis in both carotid and vertebral arteries is coupled with two missing segments of the anatomy of the circle of Willis. This is a rather extreme example but a very interesting case to illustrate the limits of the cerebral vasculature to compensate blood flow loss. In the baseline condition, the loss of CBF is approximately 15 % compared to the normal baseline flow and during the carotid endarterectomy around 40 %. Due to the severe loss in blood flow during the procedure the insertion of a shunt might be necessary to avoid temporary ischemic conditions.

One of the major challenges of the carotid endarterectomy is to determine whether a patient is insufficiently perfused during the surgical procedure. In Section 2.3, several perioperative techniques of monitoring brain activity and brain perfusion are presented. However, there is currently no method to measure the brain's actual need for oxygen. Without this information it is difficult to determine if a certain level of perfusion is sufficient to cover the oxygen demand of the brain. These monitoring techniques usually lead to an overuse of shunts. In practice it was shown that the brain has remarkable abilities to endure temporary ischemia without permanent brain damage and that in most cases a shunt is not necessary. A healthy adult under normal conditions has a CBF of approximately 50 ml/100 g/min. The unit refers to the flow per 100 g of brain tissue (based on an average brain tissue weight of 1400 g). According to [4], a severe drop in CBF during the endarterectomy from 50 to 20 ml/100 g/min (−60 %) will not damage the brain, unless prolonged over a long time. After the procedure, brain flow and all brain functions return to normal.

One important determinant of sufficient brain perfusion during the surgical procedure is the change in the brain's oxygen demand. The type of anesthesia used during the procedure has a profound influence on the brain's activity and thereby on the necessary oxygen supply. By using a local anesthesia, the patient stays fully awake and mentally active, allowing the performance of periodical communication with the patient. The brain's oxygen demand remains approximately at a normal level. In contrast, the use of a general anesthesia puts the patient in a state of unconsciousness. This leads to a decrease in the cerebral metabolic rate of oxygen ($CMRO_2$)

due to anaesthesia-induced suppression of neural activity [15]. In this case, a lower brain perfusion is efficient to match the oxygen supply to the demand.

Another method commonly used to lower the brain's oxygen consumption is to put the patient in a temporary state of moderate hypothermia before the clamping of the carotid artery. In this approach, the patient's core temperature is lowered by using cooling blankets and ice bags in the armpits and groins. There is substantial experimental evidence that moderate hypothermia decreases the cerebral metabolic rate. It is estimated that for every 1 °C decrease in core temperature the metabolic rate will be reduced by 6 % [4]. In most cases, the patient's core temperature is lowered from 37 °C to 33 °C, resulting in a 24 %-reduction of metabolic rate.

The local autoregulation mechanism presented in this work falls into the category of "short-term" regulation. This type of autoregulation mechanism reacts to sudden changes in hemodynamic and oxygen demand by adapting the vasculature within seconds. In the case of the three presented patient disease patterns, the new baseline values for flow and pressure are calculated with the short-term autoregulation model. In reality, the plaque buildup leading to the stenosis takes up to several month or even years. In this situation, a "long-term" regulation starts to develop in addition to the short-term regulation. This type of regulation leads to an actual physical reconstruction of the vasculature to meet the oxygen need of the brain tissue [1]. This means that the vaculature can adapt vessel properties (min/max compliance) to long-term changes in hemodynamic conditions and tissue oxygen demand. The calculated flow losses caused by the stenosis (new baseline values in Section 4.3) are therefore overestimated.

6 Conclusion and outlook

The motivation of this thesis was to design a reduced-dimensional model of the cerebral vasculature that has the ability to account for changes in resistance and compliance in the small arteries due to the mechanisms of autoregulation. A 0D-parameter model based on Poiseuille's Law was proposed accounting for the large cerebral arteries, arterioles, venous side, and cerebrospinal fluid circulation. The model parameters were based on literature values of average vessel geometries. Following the 0D-model was extended by a phenomenological-based autoregulation model, which adapts the vessel properties of the small arteries based on changes in CBF.
In the first step, the baseline condition was simulated. The results for flow and pressure were within the limits of reported literature values. Simulations of the autoregulatory response to an induced change in arterial pressure showed a realistic adaptation of the small vessel properties in order to restore baseline cerebral blood flow. The performance of the autoregulation was tested over a wide range of induced pressure variations. The limits of the autoregulation to maintain approximately constant CBF reflected well experimental data from the literature. In the second step, the model of the cerebral vsculature was used to simulate CBF during a surgical procedure. The compensatory capacity of the cerebral vasculature to a sudden stop in blood flow in the carotid artery during an endarterectomy was investigated. Three disease patterns with varying severity of stenosis and anatomical variation were simulated. In the case of a unilateral stenosis in combination with a complete anatomy of the CoW, the vasculature was able to almost completely compensate a sudden loss in CBF. The simulation of a severe bilateral stenosis in combination with missing parts of the CoW anatomy showed a noticeable loss in CBF after the adaption through the autoregulation.

Future work should focus on two parts of the model. First, the autoregulation model should be extended to account for the metabolic need of the brain tissue. A change in the brain's oxygen demand has a significant effect on CBF. This is especially important during general anesthesia where the brain's neurogenic activity is severely reduced, which leads to a decreased need for oxygen. Second, the 0D-representation of the circle of Willis and the proximal arteries should be expanded to include the compliance of the vessels. The large arteries are very compliant and they passively change their diameter significantly in the face of a sudden change in blood volume. This extension of the model would allow the simulation of pulsatile

flow and pressure.
The final goal of this project is to combine the cerebral autoregulation model with a 3D-representation of the large arteries. For this combination, the current model can be separated at the level of the small arteries and the 0D-representation of the large cerebral arteries is replaced with the 3D-model. The remaining 0D-model serves as a boundary condition of the 3D-model, accounting for the cerebral vasculature distal of the large cerebral arteries. This enhanced model could be used for example to simulate the influence of stenosis on CBF in more detail.

References

[1] J. E. Hall. A. C. Guyton. *Textbook of medical physiology*. Elsevier, 11th edition, 2006.

[2] J. Alastruey, K. H. Parker, J. Peiró, S. M. Byrd, and S. J. Sherwin. Modelling the circle of willis to assess the effects of anatomical variations and occlusions on cerebral flows. *Journal of Biomechanics*, 40(8):1794–1805, 2014.

[3] B. Alpers, J. Berry, and R. Paddison. Anatomical studies of the circle of willis in normal brain. *AMA Arch. Neurol. Psychiatry*, 81:409–418, 1959.

[4] R. Berguer. *Function and Surgery of the Carotid and Vertebral Arteries*. Wolters Kluwer Lippincott Williams & Wilkins, 2013.

[5] B. E. Carlson, J. C. Arciero, and T. W. Secomb. Theoretical model of blood flow autoregulation: roles of myogenic, shear-dependent, and metabolic responses. *Am J Physiol Heart Circ Physiol*, 295(4):H1572–9, 2008.

[6] K. Devault, P. A. Gremaud, V. Novak, M. S. Olufsen, G. Vernières, and P. Zhao. Blood flow in the circle of willis: Modeling and calibration. *Multiscale modeling & simulation : a SIAM interdisciplinary journal*, 7(2):888–909, 2008.

[7] U. Dirnagl and W. Pulsinelli. Autoregulation of cerebral blood flow in experimental focal brain ischemia. *J Cereb Blood Flow Metab*, 10(3):327–336, 1990.

[8] R. Fahrig, H. Nikolov, A. J. Fox, and D. W. Holdsworth. A three-dimensional cerebrovascular flow phantom. *Medical Physics*, 26(8):1589–1599, 1999.

[9] S. L. Harper, H. G. Bohlen, and M. J. Rubin. Arterial and microvascular contributions to cerebral cortical autoregulation in rats. *Am J Physiol*, 246(1 Pt 2):H17–24, 1984.

[10] F. M. Kashif, G. C. Verghese, V. Novak, M. Czosnyka, and T. Heldt. Model-based noninvasive estimation of intracranial pressure from cerebral blood flow velocity and arterial pressure. *Science translational medicine*, 4(129):129ra44–129ra44, 2012.

[11] J. Kochanowicz, G. Turek, R. Rutkowski, Z. Mariak, P. Szydlik, and J. Lyson, T. Krejza. Normal reference values of ratios of blood flow velocities in internal carotid artery to those in common carotid artery using doppler sonography. *J Clin Ultrasound*, 37:208–211, 2009.

[12] M. Lagerkranser, K. Stange, and A. Sollevi. Effects of propofol on cerebral blood flow, metabolism, and cerebral autoregulation in the anesthetized pig. *J Neurosurg Anesthesiol*, 9(2):188–193, 1997.

[13] H. Lippert and R. Pabst. *Arterial variations in man: classification and frequency*. J. F. Bergmann Verlag GmbH, KG, 1985.

[14] C. A. Lodi and M. Ursino. Hemodynamic effect of cerebral vasospasm in humans: a modeling study. *Ann Biomed Eng*, 27(2):257–273, 1999.

[15] L. Meng, A. W. Gelb, and D. L. McDonagh. Changes in cerebral tissue oxygen saturation during anaesthetic-induced hypotension: an interpretation based on neurovascular coupling and cerebral autoregulation. *Anaesthesia*, 68(7):736–741, 2013.

[16] S. Moore and T. David. A model of autoregulated blood flow in the cerebral vasculature. *Proc Inst Mech Eng H*, 222(4):513–530, 2008.

[17] K. T. Moorhead, J. G. Chase, T. David, and J. Arnold. Metabolic model of autoregulation in the circle of willis. *J Biomech Eng*, 128(3):462–466, 2006.

[18] T. W. Secomb. Theoretical models for regulation of blood flow. *Microcirculation*, 15(8):765–775, 2008.

[19] B. Spronck, E. G. H. J. Martens, E. D. Gommer, and F. N. van de Vosse. A lumped parameter model of cerebral blood flow control combining cerebral autoregulation and neurovascular coupling. *Am J Physiol Heart Circ Physiol*, 303(9):H1143–53, 2012.

[20] M. Ursino and C. A. Lodi. A simple mathematical model of the interaction between intracranial pressure and cerebral hemodynamics. *Journal of Applied Physiology*, 82(4):1256–1269, 1997.